Chemical Geology 630 (2023) 121489

Contents lists available at ScienceDirect

Chemical Geology

journal homepage: www.elsevier.com/locate/chemgeo

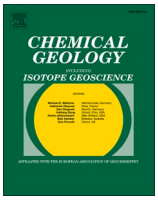

Formation of hydrocarbons favored by high pressure at subduction zone conditions

Jingyi Huang [a,b,c,d,*], Isabelle Daniel [d], Dimitri A. Sverjensky [a], Hervé Cardon [d], Gilles Montagnac [d]

[a] Dept. of Earth & Planetary Sciences, Johns Hopkins University, Baltimore, MD 21218, United States of America
[b] Dept. of Computer Sciences, University of Idaho, Moscow, ID 83844, United States of America
[c] Earth and Planets Laboratory, Carnegie Institution for Science, Washington, D.C. 20015, United States of America
[d] Univ Lyon, Univ Lyon 1, ENS Lyon, UJM, CNRS, Laboratoire de Géologie de Lyon – Terre, Planètes, Environnement UMR 5276, Villeurbanne F-69622, France

ARTICLE INFO

Editor: Dr Claudia Romano

Keywords:
Immiscible hydrocarbon fluids
Subduction zone
Deep carbon cycle
Diamond anvil cell
In situ Raman spectroscopy

ABSTRACT

Subduction zones enable carbon transport to the deep Earth. Inorganic and organic carbon in fluids released from the subducted slab are important in water-rock interactions. However, the potential role of reduced carbon species in fluids during subduction is still unclear. In particular, the pressure, temperature, and oxidation state conducive to the formation of fluid hydrocarbons are poorly understood. Here we focused on the role of pressure influencing the formation of hydrocarbons using diamond anvil cell experiments starting with 0.5 M Ca-acetate solutions over a broad range of pressures, from 1.6 to 4.6 GPa at temperatures of 300 and 350 °C. Droplets of immiscible hydrocarbon fluid coexisting with aqueous carbonate or bicarbonate and crystals of calcite or aragonite were formed at peak pressure and temperature conditions in the experiments. Greater quantities of hydrocarbons formed at higher pressure as revealed by measuring the *in situ* volume percent of the droplets. Measurement of the *in situ* Raman spectra of the co-existing aqueous solutions and analysis of the peak area ratios of acetate to HCO_3^- showed faster decrease at higher pressure, which indicated that the reactions forming hydrocarbons were accelerated by pressure. Compared to previous Na-acetate experiments at 300 °C and 3.0 GPa, this study found hydrocarbons that were more methane-rich and had more propane and less isobutane. In experiments at 350 °C, isobutane transformed to one or more aromatic hydrocarbons in an immiscible fluid. The air-dried aromatic hydrocarbons were measured using a UV laser, and show peaks of bitumen. Overall, our study supports the hypothesis that high pressures and high temperatures facilitate the possible occurrence of immiscible hydrocarbon fluids in the deep carbon cycle.

1. Introduction

The conventional wisdom is that hydrocarbon deposits in the upper crust are of biogenic origin. Biomass degradation by microbes in sediments during diagenesis forms kerogen and then thermal dissociation of kerogen forms petroleum or coal (Hunt, 1995). An abiotic origin was also proposed for conventional hydrocarbon deposits first by Dmitry Mendeleyev and then others (Mendeleev, 1877; Kudryavtsev, 1959; Kropotkin, 1997; Kenney et al., 2002; Kolesnikov et al., 2017). In the latter abiotic theory, a deep source of hydrocarbon gas from the mantle is transported vertically to the surface of the Earth. Geographical patterns of cracks in large-scale petroleum reservoirs are thought to have enabled the escape of deep gas from the mantle. The abiotic theory was further developed by Gold (1992), who claimed that the hydrocarbon gas generated at depth, while migrating upwards, became a source of nutrition for a deep subterranean biosphere leaving biomarkers in hydrocarbon fluids. The theory of a deep origin of hydrocarbons was subsequently presented in detail in Gold (2001). However, quantification of this theory has been lacking.

In contrast, considerable progress has been made in quantifying the formation of hydrocarbons from altered organic matter. For example, the thermodynamic properties of organics have been calculated in crystalline, liquid and gas phases (Helgeson et al., 1998), which provided a database for calculating the affinity of reactions involving organics, including the generation of petroleum. The reactions during kerogen maturation were modelled using a Gibbs free energy

* Corresponding author at: Dept. of Earth & Planetary Sciences, Johns Hopkins University, Baltimore, MD 21218, United States of America.
E-mail address: jyhuang@uidaho.edu (J. Huang).

https://doi.org/10.1016/j.chemgeo.2023.121489
Received 13 January 2023; Received in revised form 8 April 2023; Accepted 15 April 2023
Available online 20 April 2023
0009-2541/© 2023 Elsevier B.V. All rights reserved.

minimization (Helgeson et al., 2009). The reactions involved the incongruent melting of immature kerogen (*i.e.* partial melting of kerogen) without water to produce mature kerogen, crude oil and CO_2 gas. An earlier model found that heavy hydrocarbons, carboxylic acids and aqueous CO_2 could be metastable in oil-field fluids (Helgeson et al., 1993). However, hydrolytic reaction could alter light hydrocarbons (C9 - C2) to form even lighter hydrocarbons and aqueous CO_2 at the oil-water interface at 150 °C and 400 bars. These compounds could be used by microbes as a source of energy and nutrients (Helgeson et al., 1993).

Under crustal conditions at temperatures greater than about 500 °C, thermodynamic calculations and field observations suggest that aqueous methane can be in stable equilibrium with CO_2 (Shock, 1992; Manning et al., 2013). However, at lower temperatures, aqueous methane is kinetically inhibited from equilibrating with other carbon species (Shock, 1990). Shallow abiotic methane is often suggested to have formed by a catalytic Fischer-Tropsch type reaction (Etiope and Sherwood, 2013). The inhibition of aqueous methane equilibration permits numerous other aqueous organic carbon compounds to occur in metastable equilibrium with CO_2 depending on the redox conditions. In the classic field example, abundant acetate and other aliphatic acid anions are found in oil-field brines together with unreactive, metastable methane at 100 °C and 300 bar. Subsequently, numerous experimental studies have demonstrated metastable reversible equilibrium for many classes of aqueous hydrocarbons at temperatures of 300–400 °C and shallow crustal pressures of about 30 to 100 MPa (Shock, 1990, 1992, 1994; Seewald, 1994; Shock and Schulte, 1998; McCollom and Seewald, 2003a, 2003b; Seewald et al., 2006; Shipp et al., 2013; Venturi et al., 2017; Yang et al., 2018; Glein et al., 2020).

At upper mantle conditions, experimental observations indicate that higher pressures and temperatures appear to favor the formation of abiotic methane and other hydrocarbons (Scott et al., 2004; Foustoukos, 2012; Lobanov et al., 2013; Manning et al., 2013; McCollom, 2013; Szlachta et al., 2022; Peng et al., 2022; Tumiati et al., 2022; Toffolo et al., 2023). Experiments that included water as a major phase indicate the formation of immiscible methane-bearing hydrocarbon fluids at subduction zone pressures and temperatures. For example, in a Raman spectroscopic study of synthetic fluid inclusions trapped in quartz, immiscible hydrocarbon fluids formed from initial solutions of Na-formate only at 1.5–2.5 GPa and 600–700 °C and not at the lowest pressure of 0.2 GPa (Li, 2017). In these experiments the oxidation state was buffered by mineral assemblages. At the lowest oxidation state (*Fe−FeO*), the immiscible hydrocarbon fluid included methane (CH_4), ethane (C_2H_6), and hydrogen (H_2). At a higher oxidation state (*Ni−NiO*), CO_2, H_2O, CH_4 formed together with graphite (Li, 2017). At much higher pressures and lower temperatures of 3.0 GPa and 300 °C, immiscible hydrocarbon fluids were characterized *in situ* by Raman spectroscopy in a diamond anvil cell during experiments that started with solutions of 1.0 m sodium acetate (Huang et al., 2017). The immiscible hydrocarbon fluid consisted mainly of isobutane ($isoC_4H_{10}$) with lesser amounts of methane (CH_4), and coexisted with Na_2CO_3 crystals. Similar results were reported with sodium acetate solutions at about the same temperature and pressure (Szlachta et al., 2022). In addition, one experimental study of a more complicated system at similar conditions of 1 and 2 GPa, 550 °C started with calcite and water with silicate minerals of quartz and serpentine using the double capsule setting. The f_{O2} was buffered by iron−wüstite. *COH* fluids of mainly CH_4 and H_2O were formed and the kinetics of the experiment was enhanced by involvement of silicate and/or pressure increase (Peng et al., 2022).

Recent field and petrographic studies strongly support the existence of immiscible hydrocarbon fluids at upper mantle conditions. For example, CH_4-H_2-rich fluid inclusions were detected in the metamorphosed ophicarbonates in ultramafic rocks from the Lanzo Alpine Massifs, western Italy (Vitale Brovarone et al., 2017, 2020; Boutier et al., 2021). Even H_2S and NH_3 could be detected in the fluid inclusions in the pseudotachylyte-bearing serpentinites. The fluid inclusions were formed at depths of about 15–40 km at 400 °C during high-pressure serpentinization. CH_4-rich fluids were also found in the ultramafic rocks from the Appalachian belt in northern Vermont, USA (Boutier et al., 2021) and from Tianshan, northwestern China (Peng et al., 2021), again associated with high-pressure serpentinization. The above experimental and field evidence indicate that the formation of hydrocarbons is favored by pressures greater than about 1.0–2.0 GPa even at 400 °C. Hydrocarbons have also been noted in association with diamond-bearing rocks. For example, complex hydrocarbons up to C_{18} were detected in diamond, pyrope and olive from diamondiferous ultramafic rocks (Sobolev et al., 2019). In addition, the reduction of carboxylate was suggested during the formation of hydrocarbon fluid inclusions in diamond-forming rocks from the western Alps (Frezzotti, 2019).

Our study was designed to investigate the effect of pressure on the formation of immiscible hydrocarbon fluids at upper mantle pressures. We performed diamond anvil experiments with aqueous carboxylate solutions over a much wider range of pressure than previously investigated to 4.6 GPa at 300 and 350 °C. The pressure and temperature conditions of the experiments are plotted in Fig. 1 for comparison with a range of model subduction-zone conditions from the W1300 thermal model (Syracuse et al., 2010). Some of the experimental pressures and temperatures are within the range of the surface of subducting slabs (Fig. 1A). All the experimental pressures and temperatures are within the range of pressure-temperature paths corresponding to 7 km below the slab surface (Fig. 1B).

Our experiments started with 0.5 m calcium acetate (Ca-acetate) solutions. The reasons for selecting Ca-acetate as follows: first, the average valence state of carbon in Ca-acetate is zero, which is convenient for investigating redox reactions forming hydrocarbons and calcium carbonate (Ca-carbonate); second, Ca-carbonate rock is more geologically relevant than Na used in previous studies (Huang et al., 2017; Li, 2017; Szlachta et al., 2022); third, equations of state for calcite, aragonite, HCO_3^- and CO_3^{2-} are available at high pressures (Facq et al., 2014, 2016); fourth, aqueous bicarbonate and carbonate Raman spectra at elevated temperatures and pressures are well established over a range of temperatures and pressures (Facq et al., 2014); and fifth, Raman spectra of fluid isobutane and aqueous acetate are well established over a range of temperatures and pressures (Huang et al., 2017).

Our results suggest here that high pressure favors the formation of hydrocarbons under subduction zone conditions. Immiscible hydrocarbon fluids may therefore provide a new potential pathway for the migration of deep carbon.

2. Materials and methods

2.1. Experimental details

Experiments were performed between 1.6 and 4.6 GPa, and 300 and 350 °C, using a membrane-type diamond anvil cell (Chervin et al., 1995), with ultra-low fluorescence diamonds of 500 μm-diameter culets. The initial Ca-acetate fluid was made from $Ca(CH_3COO)_2 \bullet H_2O$ salt (laboratory grade purity, ACS reagent ≥99%) dissolved in deionized water (18 $M\Omega \cdot$ cm). The initial concentration of Ca-acetate was around 0.50 mol $\bullet$ L^{-1}.

The fluid was pressurized in a stainless-steel gasket of 75–100 μm thickness, and 150 μm diameter lined with gold 25 μm in width to prevent any reaction between the solution and the gasket. The gaskets were cleaned by sonication in detergent, and then in water, and finally soaked in highly concentrated H_2O_2 solution to remove any potential organics. The gaskets, diamond culets, diamond cell, tweezers, and needles were cleansed with cotton swabs and undusted papers with ethanol and H_2O_2. Two or three small ruby spheres were planted on the culet for pressure evaluation (Chervin et al., 2001). The cold solution of Ca-acetate was loaded in the sample chamber and the cooled cell was quickly tightly closed to avoid evaporation of the solution.

The sample was heated externally by a resistive-heating coil. A K-

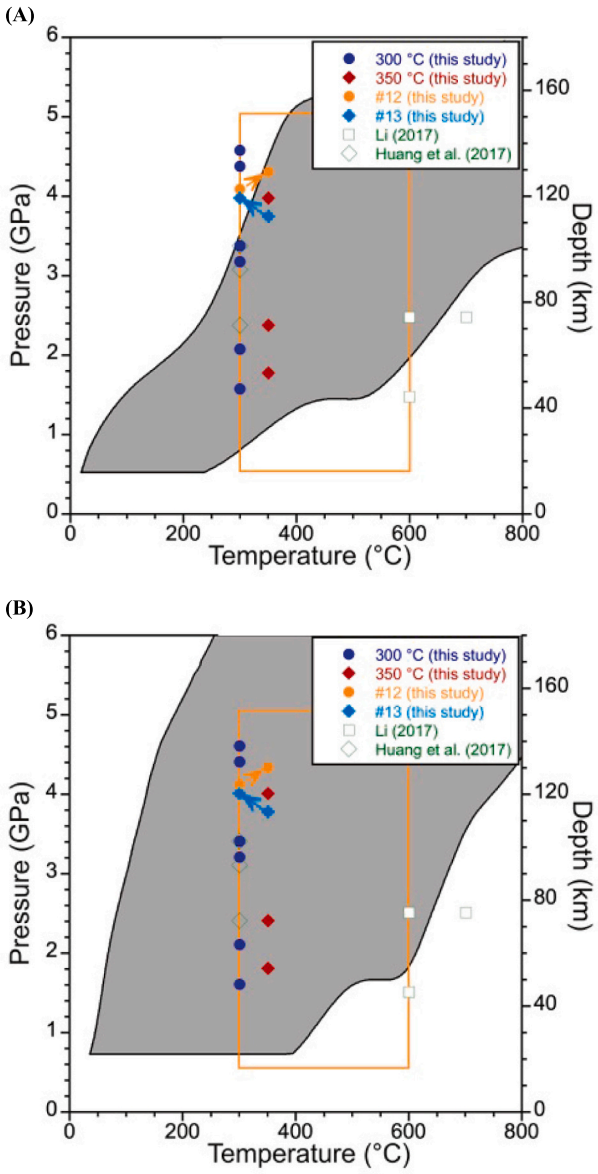

Fig. 1. Comparison of experimental pressure-temperature (P-T) conditions with geotherms of subduction zones (W1300 model in Syracuse et al., 2010). The grey area covers the P-T condition from the model at the surface of subducting slabs **(A)** and at 7 km below the surface of subducting slabs **(B).** The navy blue points represent peak pressure conditions of the current experiments at 300 °C. The red diamonds represent peak pressure conditions of experiments at 350 °C. The arrows indicate an increase in temperature (orange, #12) and a decrease in temperature (blue, #13); and end of the arrowhead shows the final P-T condition. The orange frame represents a field of calculated equilibrium constants for reactions between fluid hydrocarbons. The green empty squares and diamonds represent experiment conditions in Li (2017) and Huang et al. (2017), respectively. (For interpretation of the references to colour in this figure legend, the reader is referred to the web version of this article.)

type thermocouple inside the cell touching the anvil and the gasket measured the temperature. The uncertainty of the temperature was less than ±1 °C. Pressure was increased at a regular rate and maintained by an automatic pressure driver using He gas pumped into the cell membrane. During experiments at high pressure and high temperature, the sample pressure was calculated from the calibrated shift of the R1 fluorescence peak of the ruby, after temperature correction as previously described (Journaux et al., 2013). The exact wavenumber of R1 peak was measured together with the emission of a Ne source to minimize the uncertainty on pressure and deduced from a fit by a Pearson VI function using Peakfit® (Systat Software, San Jose, CA).

During the experiments at high pressure and high temperature, the solution, the immiscible droplets and crystals, if present, were measured *in situ* by Raman spectroscopy. The Raman instrument contains a confocal LabRam HR800 spectrometer (Horiba Jobin-Yvon) of 800 mm focal length equipped with a 532 nm Nd:YAG laser (Torus Laser, Quantum) and a Mitutoyo x20 ultra long working distance objective (0.42 N.A.). The laser power was always <10 mW and we watched for any laser damage to the sample. Raman spectra were measured with a spectral resolution of 0.3 cm^{-1}, between 300 cm^{-1} and 4100 cm^{-1} except in the range with the strong first and second order contribution of the diamond anvil.

The samples were kept at peak condition for duration between 40.7 and 141.4 h at 300 °C and 21.8 to 144.8 h at 350 °C. Under such conditions, the smallest droplets of immiscible hydrocarbon could not be systematically measured. Then the cell was quenched to about 25 °C and low pressures of about several tenths of a GPa. The Raman spectra of the aqueous solution and droplets of immiscible hydrocarbons were measured again under ambient conditions where the signals and higher spectral resolution can be obtained. It should also be noted that the wavenumbers of peaks measured after quench are different from those measured *in situ* due to substantial shift of vibration wavenumbers with changes of pressure and temperature, *e.g.*, Fig. 4 of Facq et al. (2014). Gas bubbles with hydrocarbons exsolved when the cell reached almost ambient pressure, after quenching from 300 °C. Spectra measured on the gas bubbles were of high quality and allowed measurement of methane.

Deep UV Raman Spectra were collected with a Jobin-Yvon-Horiba LabRam system with a frequency-doubled Ar^{+} laser at 244 nm and a microscope equipped with an OFR™ LMU x40 objective with a 240–360 nm broad band transmission (>80%).

2.2. Data analysis

The Raman spectra were processed by the Peakfit® (Systat Software, San Jose, CA) to subtract the baseline and obtain the values of peak areas. The Voigt function was used to fit the peaks of the solutes, hydrocarbon droplets, crystals, and gas bubbles. Raman spectra were fitted twice independently and the average values of the peak areas were used to obtain an estimate of uncertainty from standard deviation.

For aqueous HCO_3^- and CO_3^{2-} in the measured Raman spectra, their molality ratio $\frac{m1}{m2}$ can be calculated from the peak area ratio of CO_3^{2-} and HCO_3^- represented by $\frac{A1}{A2}$

$$\frac{A1}{A2} = \Lambda \frac{m1}{m2} \tag{1}$$

Where Λ is the Raman cross-section ratio of $\frac{\gamma_{CO3^{2-}}}{\gamma_{HCO3^-}}$, which is equal to 0.513 at 300 °C and 0.428 at 350 °C (Frantz, 1998) and is assumed to be independent of pressure. A variety of more recent studies have suggested a range of different possibilities for the temperature and pressure dependence of the Raman cross-section ratios (Schmidt, 2014; Pan and Galli, 2020). For consistency with our previous Raman studies of aqueous speciation (Facq et al., 2014), we used the same coefficients to calculate the molality ratio of $\frac{m1}{m2}$. For other species in the measured Raman spectra, the molality ratio was assumed as the peak area ratio due to lack of prior studies of the Raman cross-section ratio.

The carbon budget was calculated in four parts: the immiscible hydrocarbons; the aqueous C(IV) species; the crystals; and the residual acetate, which could be expressed as Eq. (2):

$$C_{tot} = C_{HC} + C_{crystal} + C_{C(IV)} + C_{acetate} \tag{2}$$

Where C_{tot} is the total carbon in the cell, C_{HC} is the immiscible hydrocarbon fluid, $C_{crystal}$is the Ca-carbonate ($CaCO_3$) crystals, C_{IV} is the aqueous C(IV) species (aqueous HCO_3^- and CO_3^{2-}), $C_{acetate}$ is the residual acetate. The value of each represents the number of moles of C.

The details of calculating the carbon budget are in section S-4 (Appendix A).

Table 1
Experimental conditions and results: pressure (GPa), temperature (°C), experiment number, duration at peak conditions (hr), crystals formed, types of immiscible hydrocarbons, alkane hydrocarbon compositions measured after quench at low frequency (wavenumber of 350–1250 cm^{-1}) and high frequency (wavenumber of 2700–3050 cm^{-1}), and bubble compositions measured after quench at high frequency (2700–3050 cm^{-1}). For compositional uncertainties see Table 2.

P	T	No.	Duration	Crystal	Types of immiscible HC	Droplet at LF	Droplet at HF	Bubble at HF
(GPa)	(°C)		(hr)			mole fraction	mole fraction	mole fraction
1.6	300	#7	141.4	calcite	alkane	0.53 C_3H_8 + 0.47 $isoC_4H_{10}$	0.33 CH_4 + 0.67 $isoC_4H_{10}$	0.20 CH_4 + 0.24 C_2H_6 + 0.29 C_3H_8 + 0.27 $isoC_4H_{10}$
2.1	300	#8	141.0	aragonite	alkane	0.42 C_3H_8 + 0.58 $isoC_4H_{10}$	0.70 CH_4 + 0.30 $isoC_4H_{10}$	0.22 CH_4 + 0.08 C_2H_6 + 0.17 C_3H_8 + 0.53 $isoC_4H_{10}$
3.2	300	#5	47.8	aragonite	alkane	Not measurable	Not measurable	0.23 CH_4 + 0.24 C_3H_8 + 0.53 $isoC_4H_{10}$
3.4	300	#0	40.7	aragonite	alkane	0.23 C_3H_8 + 0.67 $isoC_4H_{10}$ + 0.10 C_2H_6	0.58 CH_4 + 0.42 $isoC_4H_{10}$	0.19 CH_4 + 0.10 C_2H_6 + 0.14 C_3H_8 + 0.57 $isoC_4H_{10}$
4.4	300	#2	46.9	aragonite	alkane	Poor quality spectrum	Poor quality spectrum	CH_4 + C_3H_6(minor) + $isoC_4H_{10}$ [1]
4.6	300	#6	67.8	none	alkane	0.35 C_3H_8 + 0.65 $isoC_4H_{10}$	0.72 CH_4 + 0.28 $isoC_4H_{10}$	0.30 CH_4 + 0.12 C_3H_8 + 0.58 $isoC_4H_{10}$
1.8	378–350	#11	48.5	calcite	aromatic	Not measurable	Not measurable	Not measurable
2.4	350	#10	114.1	calcite	aromatic	Not measurable	Not measurable	Not measurable
4.0	350	#3	21.8	aragonite	aromatic alkane to	Not measurable	Not measurable	Not measurable
3.8–4.3	300–350	#12	144.8	aragonite	alkane + aromatic	0.59 C_3H_8 + 0.41 $isoC_4H_{10}$	0.71 CH_4 + 0.29 $isoC_4H_{10}$	Not measurable
3.8–4.0	350–300	#13	72.8	aragonite	alkane + aromatic	Not measurable	Not measurable	Not measurable

[1] Spectrum not sufficiently resolved for quantification purposes.

3. Results

3.1. Overview of experimental results

Eleven experiments were carried out. Table 1 summarizes the experimental conditions including peak pressure and temperature conditions, duration at peak conditions, minerals formed, types of hydrocarbon droplets formed, alkane hydrocarbon composition measured after quench at low wavenumber of frequency (LF) with Raman wavenumbers of 350–1250 cm^{-1} and high frequency (HF) with Raman wavenumbers of 2700–3050 cm^{-1}, and exsolved gas composition measured after quench at HF. Six experiments at 300 °C tested the effect of the peak pressure from 1.6 GPa to 4.6 GPa. Two experiments were performed at 350 °C at peak pressures of 2.4 GPa (Expt. #10) and 4.0 GPa (Expt. #3). In addition, temperature was varied between 300 and 350 °C in two experiments #12 and #13.

The general experimental results can be summarized as follows:

(1) In all experiments, within a few hours after reaching peak conditions of pressure and temperature, the aqueous species HCO_3^-, CO_3^{2-}, and residual CH_3COO^-, were detected by Raman spectroscopy. The relative amount of acetate to oxidized aqueous carbon species decreased rapidly during the first 10 to 20 h and then approached a steady state by 40 to 60 h.

(2) In all experiments, within about five hours, droplets of immiscible hydrocarbon fluid formed. When the droplets were big enough, Raman measurements indicated that it consisted of variable amounts of CH_4, C_3H_8, and isobutane ($isoC_4H_{10}$) depending on the pressure. Expressed as mole fractions, the two most abundant fluid hydrocarbon species were isobutane (0.24–0.39) and methane (0.17–0.59).

(3) During experiments at 300 °C, the alkane-bearing immiscible fluid persisted to the end of the experiments, between 40.7 up to 141.4 h for the longest one.

(4) During experiments at 350 °C, droplets of immiscible alkane-bearing fluid formed, but after several tens of hours, they became fluorescent and persisted through the end of the experiments.

(5) In one experiment with variable temperature (Expt. #12), the initial droplets of alkane-bearing fluid at 300 °C persisted for 47.7 h; the temperature was increased to 350 °C and about 65% of the droplets became fluorescent. The system reached a steady state with three immiscible fluid phases still coexisting after quenching: fluid alkane, fluorescent hydrocarbon, and aqueous solution.

(6) In the second experiment with variable temperature (Expt. #13), the first generation of droplets of immiscible alkane-bearing fluid formed at 350 °C persisted for 22 h, after which they became fluorescent. After the temperature was decreased to 300 °C, the fluorescence persisted till the end of the experiment. Only one small droplet of isobutane-bearing fluid could be detected after quench.

(7) Calcium carbonate crystals formed in all experiments except at the highest pressure (Expt. #6 at 4.6 GPa and 300 °C). Calcite crystals formed during the experiments at 1.6, 1.8, and 2.4 GPa. Aragonite formed in experiments at pressures of 2.4 to 4.4 GPa.

(8) After quenching the experiments, Raman spectra of aqueous and hydrocarbon fluids were taken, except when the latter were fluorescent.

(9) Gas bubbles were generated by exsolution at ambient temperature when the pressure was close to ambient, which enabled the quantification of CH_4, C_2H_6, C_3H_8, and $isoC_4H_{10}$ by Raman spectroscopy.

In the subsequent sections, we describe how the experimental results varied in detail with pressure and temperature.

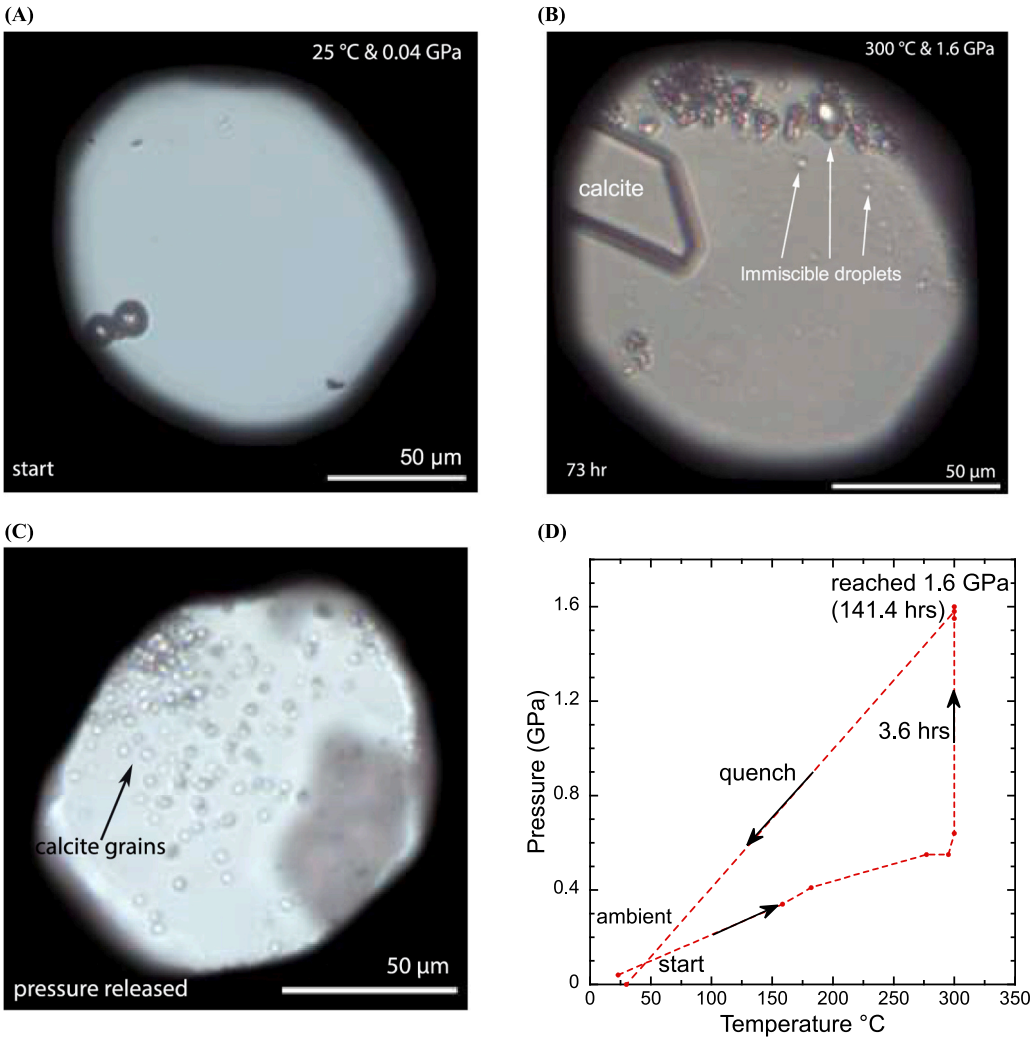

Fig. 2. Optical pictures in transmitted light of Expt. #7 in the diamond anvil cell. **(A)** The starting acetate aqueous solution and two ruby spheres as pressure gauge. **(B)** The aqueous solution, droplets of immiscible hydrocarbon fluid and a calcite crystal at 300 °C after 73 h. **(C)** After temperature quenching and pressure release, the exsolved gas filled the cell and small calcite grains precipitated from the solution. **(D)** P-T-t path of Expt. #7 at 300 °C and 1.6 GPa.

3.2. Examples of experiments at 300 and 350 °C

The experiment at 300 °C and the lowest pressure investigated, 1.6 GPa (Expt. #7), is illustrated in Fig. 2. The path of pressure and temperature during the experiment is shown in Fig. 2D. The time at which heating was started is referred to as zero. The system reached 1.6 GPa after 3.6 h. The cell stayed at peak conditions for 141.4 h and was quenched afterwards. The comparison of the *in situ* optical pictures of the diamond cell before the experiment (Fig. 2A) and at peak conditions (Fig. 2B) shows the formation of droplets of hydrocarbon fluid coexisting with calcite crystals at the expense que Ca-acetate (Fig. 2B). The bright dots on the top of the cell are the immiscible hydrocarbon fluids, the crystal is calcite.

Monitoring of the same experiment #7 by Raman spectroscopy shows that HCO_3^- appeared in the solution after 3.6 h and became stronger with time until it reached a steady state (Fig. 3A). The Raman spectra of the solution measured at 1.6 GPa and 300 °C shows that after 73.4 h, the peaks for CH_3COO^- at 936 cm^{-1}, and HCO_3^- at 1011 cm^{-1} were still strong, with a weak peak of CO_3^{2-} at 1067 cm^{-1} (Fig. 3A).

The hydrocarbon droplets measured at 1.6 GPa and 300 °C showed peaks after 76.9 h at 758 cm^{-1} and 807 cm^{-1} (Fig. 3B), characteristic of propane and isobutane, respectively. Peaks for CH_3COO^-, HCO_3^- (and a very small contribution of CO_3^{2-}) can also be seen in this spectrum due to the aqueous solution surrounding the small hydrocarbon droplet, though their intensity is too low for quantification. Overall, these spectra indicate that the reactions in the cell involved the breakdown of aqueous CH_3COO^- are disproportionation reactions that can be represented by

$$13CH_3COO^- + 3H^+ + 4H_2O \rightarrow 4C_4H_{10} + 10HCO_3^- \quad (3)$$

and

$$5CH_3COO^- + H^+ + 2H_2O \rightarrow 2C_3H_8 + 4HCO_3^- \quad (4)$$

where HCO_3^- is the example of the aqueous oxidized C-species. In Eqs. (6) and (7), part of the CH_3COO^- was reduced to form hydrocarbon fluids containing methane, propane and isobutane, and partly oxidized to form aqueous C(IV) species that lead to the precipitation of and Ca-carbonate crystals above solubility limit.

After quenching at 25 °C with the cell still under some pressure, the smaller bandwidth of the Raman peaks allowed to identify propane and isobutane peaks and even a n-butane peak in the immiscible hydrocarbon droplets (Fig. 3C). The peak at 1029 cm^{-1} in Fig. 3C could be assigned to the $C-OH$ stretching mode (ν_5) of bicarbonate. The difference of peak position from the value in Fig. 3A (1011 cm^{-1}) is consistent with a residual pressure less than the peak pressure in the quenched cell at 25 °C, based on Raman measurements for 1 m $KHCO_3$ solution at 22 °C (Frantz, 1998).

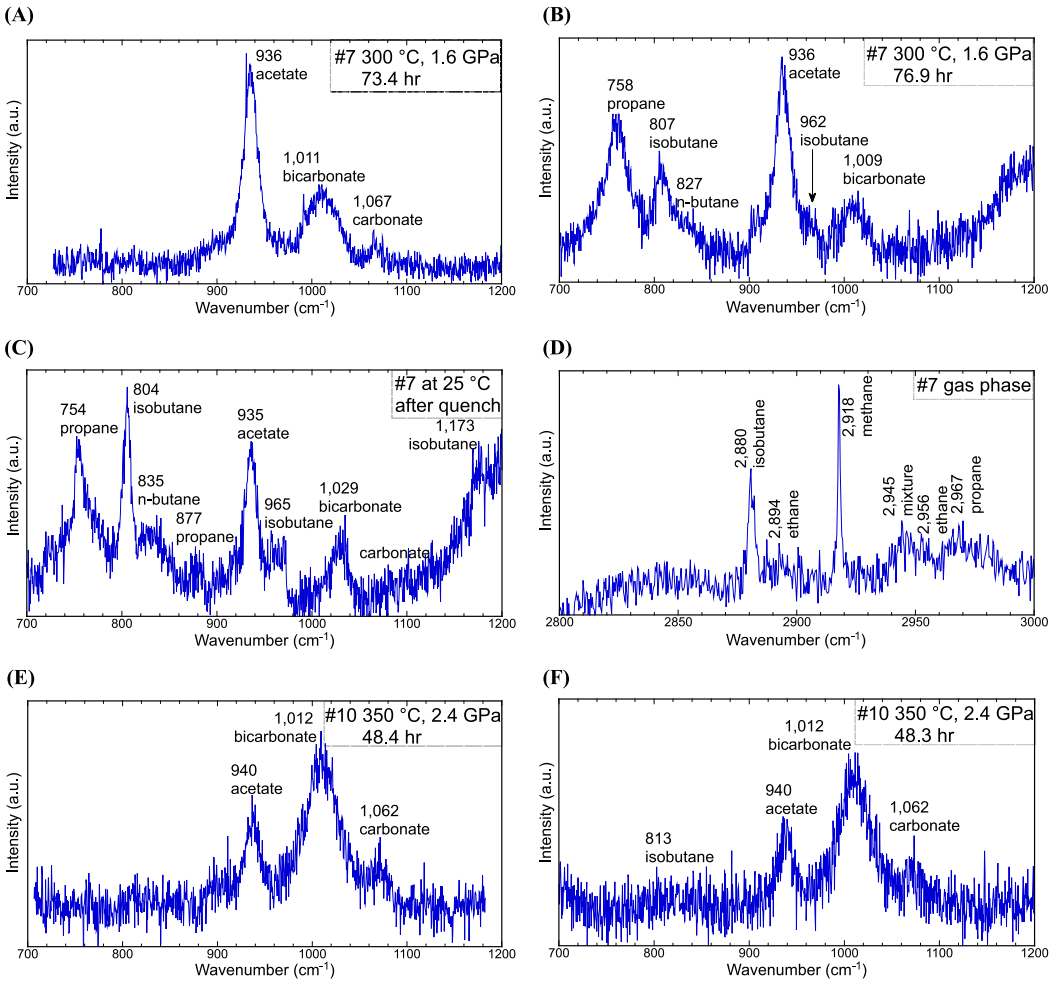

Fig. 3. *In situ* Raman spectra of aqueous solutions, immiscible hydrocarbon droplets, and the exsolved gas: **(A)** aqueous phase at 300 °C and 1.6 GPa (Expt. #7); **(B)** immiscible hydrocarbon phase at 300 °C and 1.6 GPa (Expt. #7). Some aqueous peaks appear along with the fluid hydrocarbon peaks, but it is only the strongest ones that show up, same situation as **(C)** and **(F)**; **(C)** hydrocarbon droplet at 25 °C after quenching (Expt. #7); **(D)** gas phase at 25 °C and near ambient pressure (Expt. #7); **(E)** aqueous phase at 350 °C and 2.4 GPa (Expt. #10); **(F)** immiscible hydrocarbon phase at 350 °C and 2.4 GPa (Expt. #10).

After decreasing the pressure in the cell, a large gas bubble exsolved filling the cell (Fig. 2C). The spectrum for the bubble is given in Fig. 3D and contains peaks at ~2918 cm^{-1}, ~2955 cm^{-1}, ~2967 cm^{-1} and ~2880 cm^{-1} representing methane, ethane, propane, and isobutane, respectively. Many small calcite grains also precipitated in the cell (Fig. 2C).

In experiment #10 at 350 °C, hydrocarbons characterized by a very intense fluorescence formed that prevented their analysis by *in situ* visible Raman spectroscopy. The fluorescence remained after quenching. The solution could still be measured away from droplets. Raman spectra show peaks of CH_3COO^-, HCO_3^- and CO_3^{2-} at 940 cm^{-1}, 1012 cm^{-1}, and 1062 cm^{-1}, respectively, measured at 48.4 h (Fig. 3E); the peaks of CH_3COO^- decreased with time while those of HCO_3^- and CO_3^{2-} increased in intensity. The Raman peak of the isobutane was sometimes weakly detected around 813 cm^{-1} in the droplets but couldn't be quantified (Fig. 3F). Peaks of other less abundant hydrocarbons were likely hidden in the high fluorescent background. The fluorescence induced by the visible laser at 532 nm is often the signature of aromatics in such a system and could be confirmed by the analysis of experiment #11 by deep UV Raman spectroscopy. No further information on the composition or structure of the aromatic hydrocarbon was obtained in this study. The co-existence of aromatic and alkane hydrocarbons suggested that aromatics could be formed from alkanes, which will be described based on the two experiments with changing temperatures (section 3.3.5).

3.3. Kinetic effects of pressure and temperature

3.3.1. Aqueous fluid chemistry and Ca-carbonate mineral formation

The breakdown of CH_3COO^- was monitored during the experiments by measuring *in situ* the Raman spectra of the aqueous fluid with time that showed the decay of CH_3COO^-, and the formation of HCO_3^-, and CO_3^{2-}. Fig. 4A represents the selected Raman spectra measured at 3.2 GPa and 300 °C (Expt. #5). The starting solution showed the intense C—C symmetric stretching peak of acetate. After 3.73 h of heating, the C—O stretching peaks of HCO_3^- and CO_3^{2-} became visible, around 1020 cm^{-1} and 1065 cm^{-1}, respectively. Two weak peaks around 770 cm^{-1} and 820 cm^{-1} of propane and isobutane also appeared. The C—C peak of acetate decreased in intensity while those of HCO_3^- and CO_3^{2-} increased with time. The changes of the solution spectra in Expt. #10 at 2.4 GPa and 350 °C (Fig. 4B) are similar to those for Expt. #5.

The areas of the CH_3COO^- and HCO_3^- Raman vibrations at *ca.* 940 and 1020 cm^{-1}, respectively, were used to calculate the peak area ratio of $CH_3COO^-/(1+n)HCO_3^-$ as a proxy of the reaction/oxidation rate, where n is the relative amount of CO_3^{2-} to HCO_3^- measured from dissolved aragonite in water (Facq et al., 2014). The peak area ratios of $CH_3COO^-/(1+n)HCO_3^-$ of selected experiments at 300 and 350 °C as a function of time are depicted in Fig. 5. The error bars represent uncertainties obtained from analyzing independently twice the noisy high-temperature Raman spectra.

It can be clearly seen in Fig. 5 that the proxy deduced from Raman

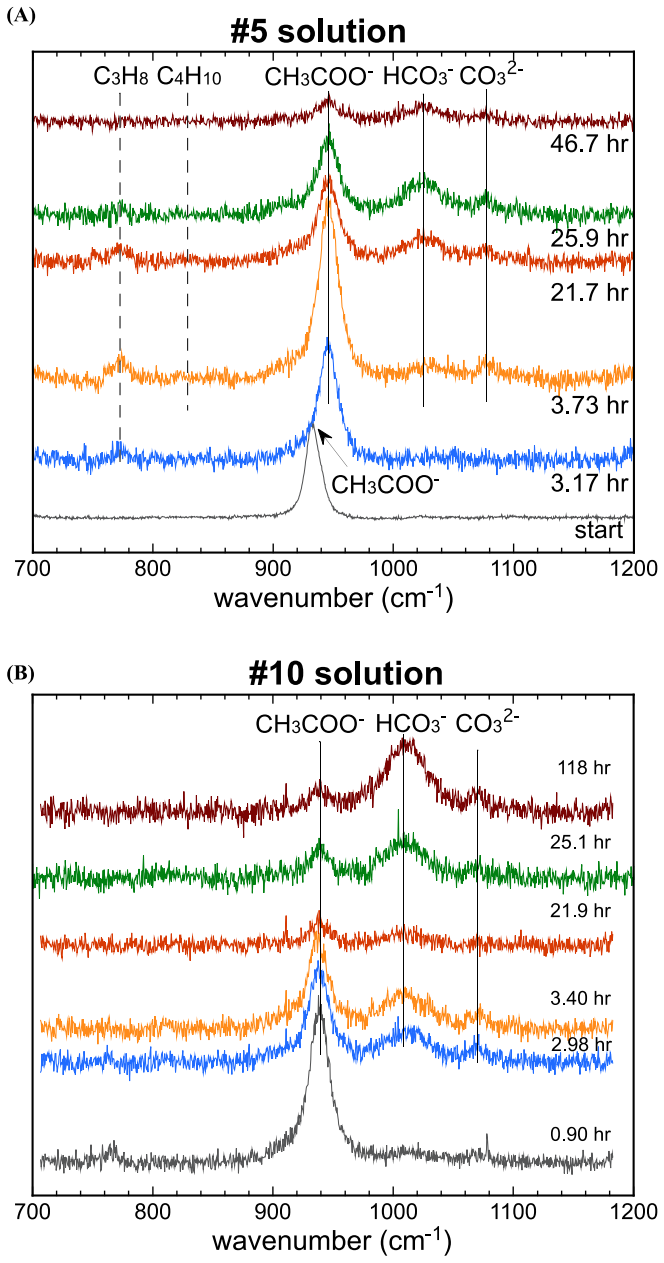

Fig. 4. Raman spectra of aqueous solutions as a function of time: **(A)** at 300 °C and 3.2 GPa (Expt. #5); **(B)** at 350 °C and 2.4 GPa (Expt. #10).

measurements shows systematic decreases with time from a high value of about 40 when first measured at 1 h to a as little as 0.1 after tens of hours at peak conditions. It should be emphasized that the proxy doesn't provide the absolute quantity of acetate with time, only the relative concentrations of species can be extracted from the ratios of the peak areas of the species. However, we noticed from analysis of the Raman peak areas that the proportion of the CH_3COO^-peak area relative to the sum of the peak areas of CH_3COO^- and $(1+n)HCO_3^-$ decreased linearly with time. Because the lower part of the ratio $CH_3COO^-/(1+n)HCO_3^-$ only relates to HCO_3^-, we assumed that the increase of HCO_3^- is also linear with time. The overall fitting function for the experimental ratios of $CH_3COO^-/(1+n)HCO_3^-$ is given by the fraction of two linear functions of time.

The smooth solid curves in Fig. 5 represent the fit of our empirical equation to the experimental data and facilitate a comparison of the apparent relative rates of breakdown of acetate to oxidized aqueous C-species. We found that the peak area ratio of $CH_3COO^-/(1+n)HCO_3^-$ decreases faster and became asymptotic to the x-axis in experiments at both higher pressures and higher temperatures. Therefore, our results are displayed in three separate figures in Fig. 5 to show the effect of pressure and temperatures.

Fig. 5A and B refer to experiments at 300 °C. In Fig. 5A, it can be seen that the curve at 1.6 GPa (Expt. #7) decreases faster initially than the curve at 3.2 GPa (Expt. #5) but subsequently stays flat at a higher value, even after 145 h. In Fig. 5B, the curve at 4.4 GPa (Expt. #2) decreased faster than the curve at 4.0 GPa (Expt. #12); both decreased faster than the curves at lower pressure (Fig. 5A) during the first 20 h and stabilized at a lower steady-state value. In Fig. 5C, representing experiments at 350 °C, the curves obviously decreased much faster than the curves at 300 °C. Although Expt. #3 in Fig. 5C at 4.0 GPa only lasted for 27 h, it reached a very low ratio of $CH_3COO^-/(1+n)HCO_3^-$ equal to about 0.1 after 20 h, a value only reached at 300 °C after 45 h (Fig. 5B). Overall, these results clearly demonstrate a strong effect of pressure and of temperature on the breakdown of aqueous acetate.

To further investigate the specific roles of pressure and temperature, the experimental ratios of $CH_3COO^-/(1+n)HCO_3^-$ from Fig. 5A-C were plotted as a function of pressure at selected time intervals in Fig. 6A-C. For convenience, the data were grouped as 5 ± 2 hours (Fig. 6A), 25 ± 5 hours (Fig. 6B) and at 45 ± 4 hours (Fig. 6C). Most of the data at 300 °C are represented by the blue dots. Data at 350 °C are represented by red diamonds. The blue dashed curves represent smooth trends interpreted through the data for 300 °C. Despite the scatter in the data, it can be seen that the ratio $CH_3COO^-/(1+n)HCO_3^-$ decreases asymptotically with pressure, indicating that pressure favors the breakdown of CH_3COO^-.

It is also noteworthy in Figs. 6A-C that the few experiments carried out at 350 °C show trends consistent with those at 300 °C, but are shifted systematically to lower ratios of $CH_3COO^-/(1+n)HCO_3^-$ compared to the data at 300 °C. The ratios at 350 °C are also smaller than those at 300 °C and over a shorter time interval, which indicates that temperature as well as pressure accelerated the reaction.

Crystals of calcite or aragonite appeared before 23 h in almost all the experiments. Only at the highest pressure investigated in Expt. #6 did no crystals form, presumably due to the very high solubility of aragonite at this high-pressure condition.

3.3.2. *Calculated pH values of the aqueous phase*

The *pH* of the aqueous phase in the experiments could also be assessed using the results obtained above using the equilibrium dissociation constant for the reaction.

$$HCO_3^- = H^+ + CO_3^{2-} \quad (5)$$

The details of calculating the *pH* are given in section S-5 (Appendix A). We assume a steady state has been reached by the end of the experiments. It should be noted that there was no carbonate crystal precipitated at 4.6 GPa, which probably caused more CO_3^{2-} to remain in the solution and therefore resulted in the higher *pH* at 4.6 GPa. The change of *pH* with pressure are presented in Fig. 7 for 5 ± 2 hours (Fig. 7A), 25 ± 5 hours (Fig. 7B), and 45 ± 4 hours (Fig. 7C) at 300 °C and 350 °C. *pH* decreased with pressure, overall, even at 25 ± 5 h with the largest scattering. The slope of the decrease is larger at 300 °C than at 350 °C and *pH* became very close at 25 ± 5 h and 45 ± 4 h. Despite fewer data at 350 °C, the *pH* values seem lower than at 300 °C for pressures <3.0 GPa in Fig. 7A-C. For pressures >3.0 GPa, the difference of *pH* between 350 °C and 300 °C seems similar within uncertainty. If we had used the Raman cross-section ratio Λ (see section 2.1) from Pan and Galli (2020), the calculated *pH* would still decrease with pressure, with a slope slightly flattened by <1%.

3.3.3. *Immiscible hydrocarbon fluid quantities at peak conditions*

Besides aqueous C(IV) species, droplets of immiscible hydrocarbon fluids are the other main products of the reactions represented by Eqs. (6) and (7). The volume percentages of the droplets plotted in Figs. 8A -

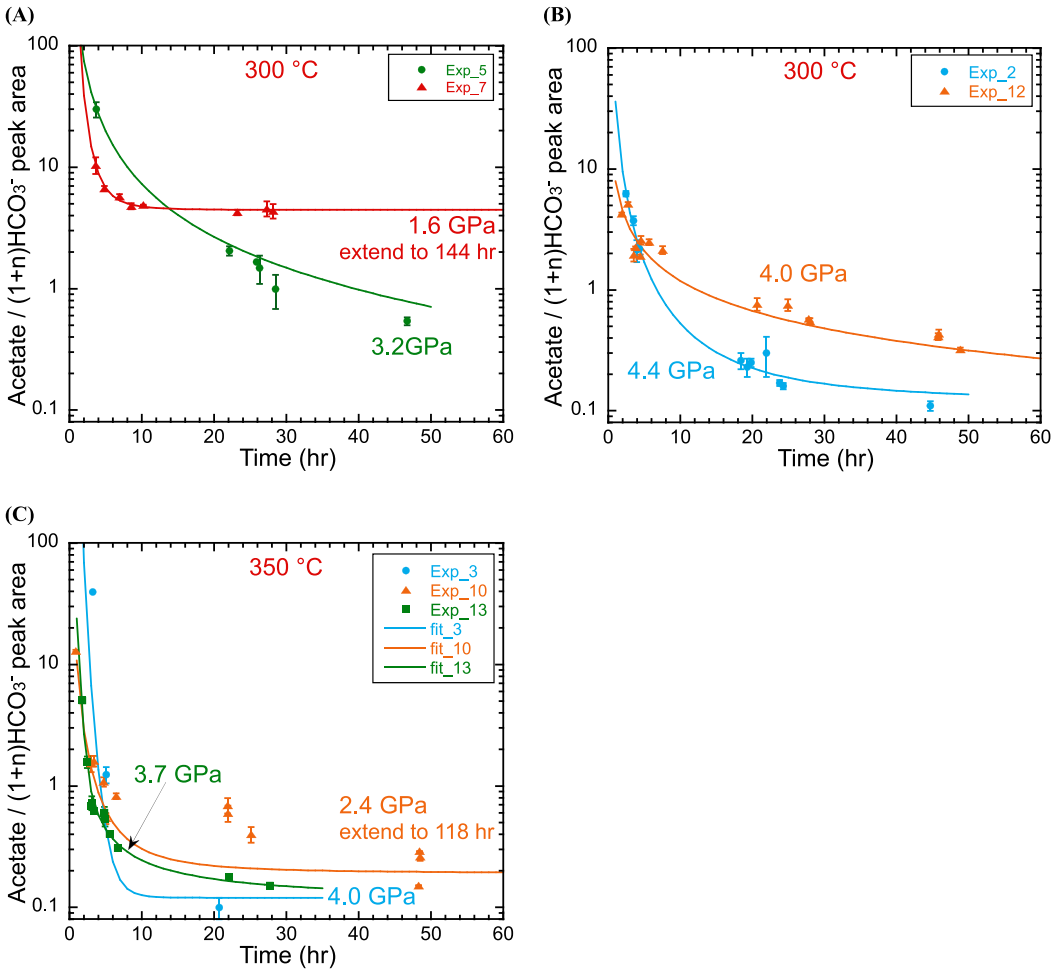

Fig. 5. Breakdown of acetate during experiments at **(A)** 300 °C and 1.6 & 3.2 GPa, **(B)** 300 °C and 4.0 and 4.4 GPa, **(C)** 350 °C and 2.4, 3.7 and 4.0 GPa. The curves represent fitting to the data (see section 3.3.1). The n value corresponds to the molar ratio of CO_3^{2-}/HCO_3^-, from relative amounts of dissolved CO_3^{2-} and HCO_3^- in Facq et al. (2014).

C were derived from measurements of *in situ* photographs taken at 300 °C and 350 °C, over a wide range of pressures at three different time intervals during the experiments: 5 ± 2 (Fig. 8A), 25 ± 5 (Fig. 8B), and 45 ± 4 hours (Fig. 8C). After only 5 h, it can be seen that there is no further trend apparent with pressure (Fig. 8A). However, at the longer time intervals referred to in Figs. 8B and C, it can be seen that the volume percent of hydrocarbon fluids tends to increase with pressure at 300 °C and 350 °C. The dashed curves were drawn to approximate trends of the data in Figs. 8B and C. The systematic increase of the amount of hydrocarbon fluid with pressure is similar to the systematic decrease of the ratio of CH_3COO^-/HCO_3^- in the aqueous fluid (Fig. 5). However, unlike the changes in the aqueous phase, there is no difference between the pressure-dependence of the volumes of the hydrocarbon fluid at 300 *versus* 350 °C (Figs. 8A-C).

3.3.4. *Composition of hydrocarbon droplets at peak conditions and after quench*

In many experiments the immiscible fluid hydrocarbon droplets were too small to be measured with Raman spectroscopy at peak conditions. However, droplets larger than 5 μm formed in some experiments and were large enough to enable measurement of propane and isobutane with high resolution at peak conditions (Fig. 3B, Expt. #7). Whenever measured, the relative peak areas of propane and isobutane was calculated and considered as a first approximation to the relative numbers of moles of propane and isobutane, expressed as mole fractions.

After quench, the sharper Raman peaks in the Raman spectra of the hydrocarbon fluid droplets enabled quantification of the peak areas of additional hydrocarbon compounds from experiments at 300 °C. Peak areas for ethane, propane, and isobutane were again obtained from the low frequency part of the Raman spectra and peak areas for methane and isobutane were measurable at high frequency. The detailed peak assignments are described in Appendix A. These measurements enabled quantification of the relative peak areas for up to four hydrocarbon species. We again assumed that the relative peak areas approximate the relative numbers of moles of the hydrocarbon species, which can be expressed as mole fractions. For four key experiments, #7, 8, 0, and 6, in order of increasing pressure, the measured hydrocarbon fluid compositions including the relative amounts of methane, ethane, propane and isobutane were used in the overall carbon budget (see below). They are given in Table 2 and reported in Fig. 9A. It can be seen that, at pressures >1.6 GPa, methane is the major species in the hydrocarbon fluid (48 to 59 mol%). The fraction of isobutane is greater than that of propane for pressures of 2.0 GPa and higher; in fact, by this measure, propane represents only 12 to 18 mol% of the total hydrocarbon fluids.

This outcome is consistent with the results for the exsolved gas measurements reported in Fig. 9B. The compositions of gas bubbles were obtained by fitting the area of C—H stretching Raman peaks in the high frequency range from 2700 to 3050 cm^{-1}. It can be seen in Fig. 9B that the proportion of isobutane increases with pressure, and methane slightly increases, but ethane and propane decrease. However, the proportions of the different hydrocarbons in the gas bubble probably also reflect the solubility of the gases at ambient temperature and low but not

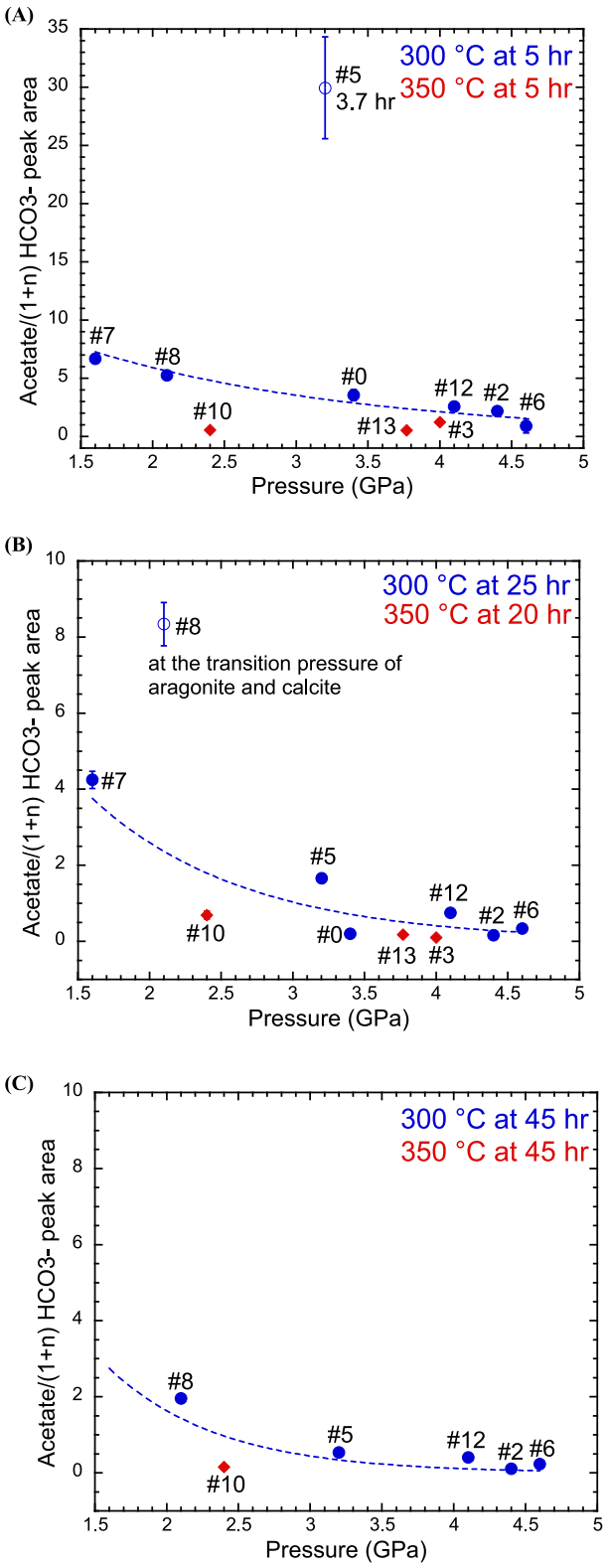

Fig. 6. The breakdown of acetate as a function of pressure at 300 °C (blue) and 350 °C (red) at time steps of **(A)** 5 ± 2 h, **(B)** 25 ± 5 h, and **(C)** 45 ± 4 h. The circles and diamonds represent the ratio of acetate to HCO_3^- from Raman measurement. Open circles represent anomalous measurements. (For interpretation of the references to colour in this figure legend, the reader is referred to the web version of this article.)

ambient pressure.

Some data for *in situ* pressures and temperatures are shown in Fig. 9C. It should be noted that measurement of methane was in general not possible at peak conditions in the hydrocarbon fluids. Despite the small number of data points in Fig. 9C, the data suggest that the proportions of isobutane and propane change from propane-rich below 2.0 GPa to isobutane-rich fluid above 2.0 GPa. This result is qualitatively consistent with the quench data shown in Figs. 9A and B.

In the experiments at 350 °C, before the alkane-bearing droplets became fluorescent, Raman spectra could be obtained. The results can be seen in Fig. 9D, which again shows that isobutane was more abundant than propane. Even after quenching, the laser-induced fluorescence on the hydrocarbon droplets prevented any Raman measurement. The quenched products of Expt. #11 deposited on the diamond anvil could be measured by deep UV Raman spectroscopy. The spectrum showed weak D band at 1385 cm^{-1} and 1431 cm^{-1}, and a strong G band at 1607 cm^{-1} (Fig. 9E) characteristic of very immature kerogen (Quirico et al., 2020). The bands at 1080, 1431, and 1721 are from the calcite crystals (Hollis et al., 2021). These results provide supporting evidence that the immiscible hydrocarbon fluids that formed at 350 °C likely contained a significant amount of at least one aromatic hydrocarbon, consistent with the observed fluorescence under peak conditions. Furthermore, the fluorescent hydrocarbons formed at peak conditions after an initial alkane-bearing immiscible hydrocarbon fluid had formed. The relationship between the two hydrocarbon fluids is discussed below.

3.3.5. *Fluid hydrocarbon transformations at peak conditions*

To investigate the relative stabilities of the alkane and aromatic hydrocarbon droplets, two experiments were performed during which the temperature was changed. In Expt. #12, the temperature was increased to 350 °C after 47.7 h at 300 °C. In Expt. #13, the temperature was decreased to 300 °C after 27.9 h at 350 °C. The associated change in pressure was relatively modest: in Expt. #12, the pressure was increased from 3.8 to 4.3 GPa and in Expt. #13 the pressure was increased from 3.8 to 4.0 GPa (Table 1).

In Expt. #12, abundant droplets of immiscible alkane-bearing fluid were present during the first 47.7 h at 300 °C (Fig. 10A). After increasing the temperature to 350 °C, many of the droplets changed and became highly fluorescent (marked in green in Fig. 10B). While most of the larger alkane droplets became aromatic, the smaller ones stayed non-fluorescent, but the intensity of the alkane hydrocarbon peak was weak. Altogether, about 65% of the initial alkane droplets became aromatic after reaching 350 °C. Eventually the system reached a steady state with three phases of fluids coexisting: an alkane fluid; an aromatic hydrocarbon fluid; and an aqueous solution. This situation persisted for 97.1 h until the experiment was quenched. It is noteworthy that the fast progression of an alkane fluid to an aromatic hydrocarbon fluid observed in detail in this experiment reflects what happened in the fixed temperature experiments at 350 °C, discussed above. This progression strongly suggests that the reaction forming the aromatic hydrocarbon starts from the alkane-bearing fluid.

In Expt. #13, initially at 350 °C and 3.7 GPa for 27.9 h, alkane-bearing droplets containing propane and isobutane formed first (at 3.2 h). After 22 h, the droplets became fluorescent and stayed that way after the temperature was decreased to 300 °C at 27 h (Fig. 10C). After quench, non-fluorescent alkane hydrocarbon was detected in a small droplet. The ratio of the peak areas of propane and isobutane to HCO_3^- were 0.0052 and 0.038, respectively, implying a propane to isobutane ratio of 0.14, which is lower than the results in Table 2 for Expts. #0 and #6. The individual droplets were systematically smaller than those in Expt. #12 and the overall volume percent of fluid hydrocarbon was smaller than in Expt. #13. One reason could be that the peak pressure of Expt. #13 was lower than in Expt. #12. The duration of the peak condition of Expt. #13 was shorter than Expt. #12 because the reactions were faster with higher temperature. Overall, the latter experiments showed that the alkane hydrocarbon fluid could partly transform to and

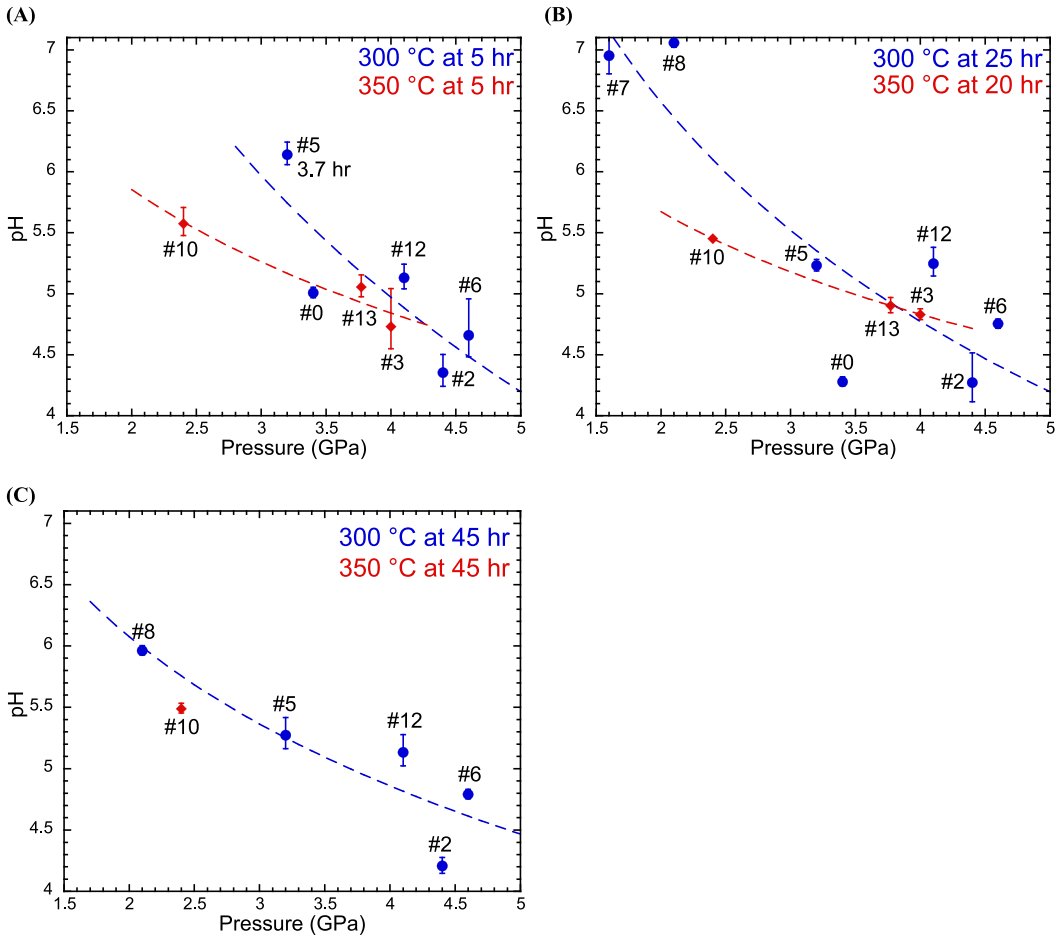

Fig. 7. Theoretical calculation of pH with pressure at 300 °C (blue dots) and 350 °C (red diamonds) at time steps of **(A)** 5 ± 2 h, **(B)** 25 ± 5 h, and **(C)** 45 ± 4 h. The dashed curves are guides for the eye. The neutral pH is systematically lower than the calculated pH at experimental P-T conditions. (For interpretation of the references to colour in this figure legend, the reader is referred to the web version of this article.)

then co-exist with an aromatic hydrocarbon fluid following temperature increase from 300 to 350 °C, and that this transformation was not reversible.

3.4. Carbon budget

The carbon budget for the experiments at 300 °C was calculated by estimation of the fraction of carbon in each phase: the hydrocarbon droplets, the aqueous solutions and the crystals. Pie graphs of the carbon budget expressed as mol% of the total carbon in the cell are presented in Figs. 11A - C. The compositions of the hydrocarbon droplets were calculated using the quenched Raman spectra (Table 2) and are presented as the zoomed pie graphs on the right-hand side of Figs. 11A - C. The compositions of the aqueous C(IV) species were calculated using the Raman spectra at peak conditions, converted from the measured ratio of the peak areas of HCO_3^- and CO_3^{2-} in Eq. (1), and are presented as the zoomed pie graphs on the left-hand side of Figs. 11A - C.

At the lowest pressure (1.6 GPa, Fig. 11A), a considerable amount of aqueous acetate still persists through the experiment (45% of the total carbon). A similar amount of carbon is in the hydrocarbon fluid (33%), and a smaller amount is in the form of oxidized aqueous carbon species (21%). The calcite crystal takes up only ~1% of total carbon. The overall decomposition reaction of this experiment can be expressed by Eq. (6) as

$$27.5CH_3COO^- + 1.0Ca^{2+} + 11H_2O \rightarrow 2.0CH_4 + 4.6C_3H_8 + 4.3C_4H_{10} + 14.7HCO_3^- + 6.3CO_3^{2-} + 1.0\,CaCO_3^{calcite} + 1.8H^+ \quad (6)$$

where aqueous Ca^{2+} is used to balance the formation of the aragonite crystal.

At intermediate pressure (3.4 GPa, Fig. 11B), less residual acetate was present at the end of the experiment (33%), and greater amounts of hydrocarbon fluid (39%) and oxidized aqueous carbon species (20.4%) are formed, whereas aragonite accounted for 7.5% of the total carbon. The overall decomposition reaction of this experiment can be expressed by Eq. (7) as

$$33.7CH_3COO^- + 7.5Ca^{2+} + 16.3H_2O \rightarrow 8.0CH_4 + 0.9C_2H_6 + 2.0C_3H_8 + 5.9C_4H_{10} + 18.2HCO_3^- + 2.2CO_3^{2-} + 7.5CaCO_3^{arg} + 1.7H^+ \quad (7)$$

At the highest pressure (4.6 GPa, Fig. 11C), it can be seen that almost all the acetate was decomposed to form hydrocarbon droplets and aqueous C(IV) species, with only 8% of the total carbon remaining as acetate. No crystal of aragonite formed at these conditions, presumably because the very high solubility of aragonite at this pressure. The overall decomposition reaction in this experiment can be expressed by Eq. (8) as

$$46CH_3COO^- + 25\,H_2O \rightarrow 15CH_4 + 4.3C_3H_8 + 6.2C_4H_{10} + 12HCO_3^- + 27CO_3^{2-} + 20H^+ \quad (8)$$

Comparing the three pie charts, it can be seen that, from 1.6 to 4.6 GPa, the fraction of the total carbon present in hydrocarbon fluid increased by 20 mol%. The carbon in aqueous C(IV) species also increased by 18 mol%, resulting in almost no residual acetate at 4.6 GPa and more hydrocarbon fluid at higher pressure. The proportion of total carbon in isobutane varied between about 50 to 60% but the proportion

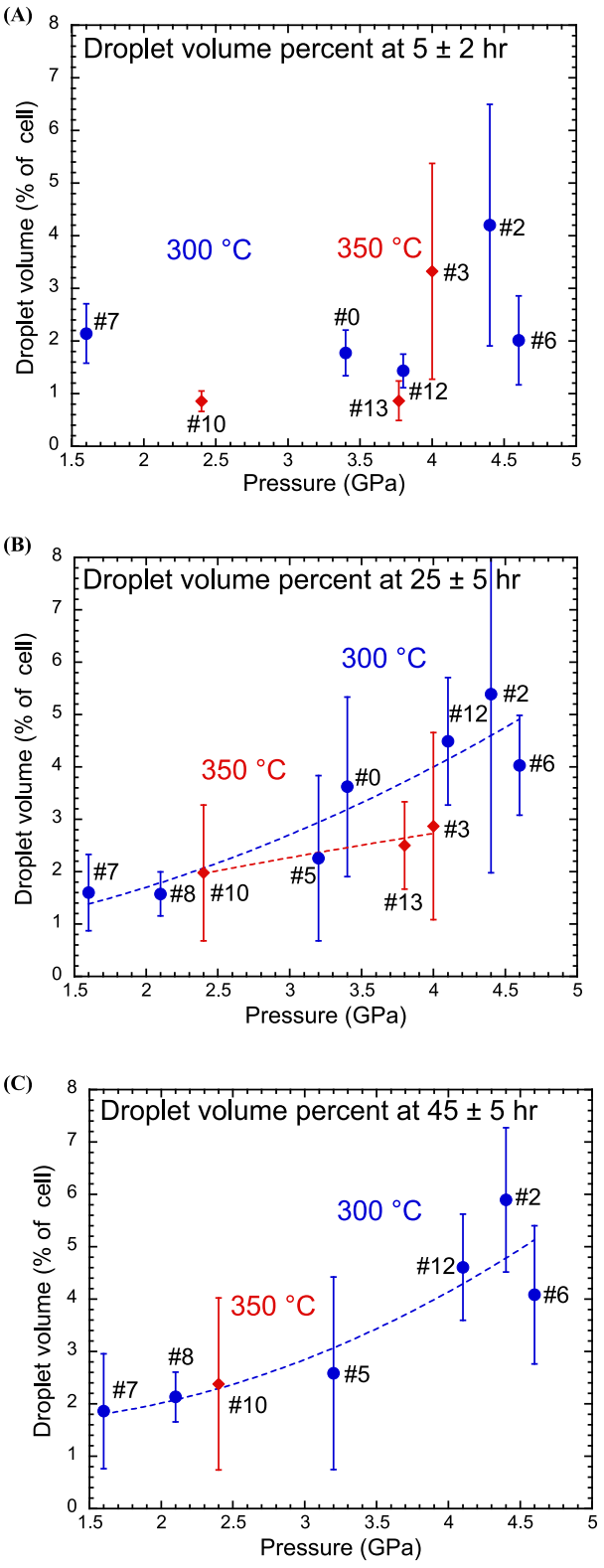

Fig. 8. The volume percent of immiscible hydrocarbon in the cell with pressure and time. Dashed curves represent the trends of the data points: **(A) - (C)** as a function of pressure at 5 ± 2 h, 25 ± 5 h, and 45 ± 4 h (300 °C, blue dots, 350 °C, red diamonds). (For interpretation of the references to colour in this figure legend, the reader is referred to the web version of this article.)

of total carbon in methane increased with increasing pressure to about 30%, suggesting that increasing pressure was associated with a decrease in the overall valence of carbon in the hydrocarbon fluid (*i.e.* the hydrocarbon fluid became more reduced with increasing pressure). In addition, in the aqueous phase, the switch from HCO_3^- to CO_3^{2-} with increasing pressure is consistent with the known pressure dependence of bicarbonate dissociation at high pressures (Facq et al., 2014).

4. Discussion

4.1. Comparison with Na-acetate solutions at 300 °C and ~ 3 GPa

Our experimental results for 0.50 M Ca-acetate solutions at 3.4 GPa and 300 °C can be directly compared with results for 1.0 m Na-acetate solutions at ~3 GPa and 300 °C (Huang et al., 2017). The two sets of experiments are comparable since they used the same total acetate starting concentration and the same experimental techniques. In both studies, CH_3COO^- with carbon in oxidation state zero disproportionated to form aqueous HCO_3^- and CO_3^{2-} species and carbonate crystals with carbon in oxidation state +4, and immiscible hydrocarbon fluids containing $isoC_4H_{10}$, C_3H_8, and CH_4 with carbon in oxidation states −2.5, −2.67, and − 4.0, respectively. However, there are a number of important differences between the Na- and the Ca-acetate systems.

In the Na- and Ca-acetate experiments, although very similar total amounts of aqueous oxidized C-species formed, the proportion of HCO_3^- to CO_3^{2-} that formed in the Na-acetate experiments (~1.7) was much lower than in the Ca-acetate experiments (~8.1). Assuming aqueous equilibrium between these two species according to Eq. (5), this observation indicates that the *pH* of the Ca-acetate experiment at peak conditions was lower, by about 0.7 log units at 3 GPa and 300 °C. This is consistent with the expected lower solubility of $CaCO_3$ relative to Na_2CO_3, a feature that is also manifested by the much larger amount of carbon precipitated as $CaCO_3$ (7.5% of total C as aragonite at this temperature and pressure) compared to Na_2CO_3 (~1% of the total C). Overall, the Na- and Ca-systems led to very similar amounts of oxidized aqueous C-species, but a greater amount of carbonate mineral formed in the Ca-system.

With respect to the hydrocarbon fluids in the Na- and Ca-systems, the total amounts of carbon in fluid hydrocarbons formed in the two systems are very similar. However, the amounts of carbon (out of the total carbon) in the different hydrocarbons were significantly different. For example, methane took up only about 9–10% of the total carbon in each system, but propane was very minor in the Na-system while it took up about 6% in the Ca-system. Isobutane took up about 47% of the total carbon in the Na-system, but only 25% in the Ca-system at 3 GPa and 300 °C. Isobutane took up about the same percentage of the total carbon at the highest pressure (Fig. 11C), but methane took up 15% of the total carbon. Overall, the average oxidation state of C in the hydrocarbon fluid was similar in both systems, about −2.85 in the Na-system and −2.9 in the Ca- system.

4.2. Comparison with high pressure hydrocarbon experiments

Experiments forming immiscible hydrocarbons have also been carried out with Na-formate solution at higher temperature and lower pressure, at 600 to 700 °C and 1.5 to 2.5 GPa (Li, 2017). The hydrocarbons were trapped in synthetic fluid inclusions in quartz and analyzed at ambient temperatures. During the experiments, oxygen fugacities (f_{O2}) were buffered at four different degrees. At the lowest f_{O2} (*Fe−FeO* buffer), CH_4 and C_2H_6 were formed without graphite. At the intermediate f_{O2} (*Ni−NiO* and *Co−CoO* buffer), CH_4 and CO_2 were formed with graphite. At the highest f_{O2} (*Re−ReO*$_2$ buffer), only CO_2 formed with graphite. These experiments indicated that the formation of graphite in the presence of an immiscible hydrocarbon fluid depends on f_{O2}. No hydrocarbons with carbon number greater than ethane were reported, which contrasts with our experiments at 300 °C, in which

significant amounts of propane and isobutane formed.

Interestingly, no graphite formed in our experiments, even though the C in graphite has the same average valence state of acetate. Preliminary mass transfer models indicate that the aqueous fluids in the experiments were strongly supersaturated with respect to graphite. Therefore, the lack of graphite in the experiments is almost certainly attributable to a kinetic inhibition of graphite formation at the relatively low temperatures of our experiments, *e.g.*, Manning et al. (2013). For example, in experiments starting with $FeCO_3$ and water at 200 and 300 °C, 0.05 GPa, H_2 and CO_2 were formed in the fluid and a condensed graphene-structure carbon formed a coating on the mineral with a thickness of <1 nm (Milesi et al., 2015). Ordered graphite did not form under these conditions. Even at higher pressures and temperatures of 1 GPa and 600 °C, only poorly ordered graphite was formed along with aqueous silica, CH_4 and H_2 (Foustoukos and Stern, 2012). Such experiments contrast with the apparent formation of crystalline natural graphite at 500 °C and f_{O2} buffered by QFM in propylitic hydrothermal altered volcanic rock (Luque et al., 2009).

Another experiment studied the solubility of graphite-containing synthetic carbonaceous material at 1 GPa and 550 °C and found that the content of crystalline graphite as well as the surface properties, such as the type of active sites and the proportion of sp2-and sp3-hybridized carbon could influence kinetic effects, which could generate different results between thermodynamic predictions and experiments (Toffolo et al., 2023). The apparent difference between experiments, natural systems, and thermodynamic predictions may reflect different kinetic regimes, or different water-rock ratios, or different water activities. Overall, these experiments indicate the potential importance of immiscible hydrocarbon fluids under subduction-zone conditions.

4.3. Trends with pressure at 300 °C as a result of acetate breakdown to hydrocarbons

In the aqueous phase, as pressure increases from 1.6 to 4.6 GPa the breakdown of acetate is favored, as indicated by the ratio $CH_3COO^-/(1+n)HCO_3^-$ (Figs. 6A-C). Neglecting the minor amount of CO_3^{2-} produced, we can write the reaction as

$$CH_3COO^- + 4H_2O = 2HCO_3^- + H^+ + 4H_{2,aq} \quad (9)$$

The logarithm of the equilibrium constant for this reaction can be written as

$$logK = log\left(\frac{\left(a_{HCO_3^-}\right)^2}{a_{CH_3COO^-}}\right) + 4log\left(a_{H_{2,aq}}\right) - \mathrm{pH} \quad (10)$$

and *logK* is displayed as a function of pressure and temperature in Fig. 12A. It can be seen that increasing pressure favors the persistence of aqueous acetate relative to aqueous bicarbonate, whereas increasing temperature favors aqueous bicarbonate. However, such trends assume constant *pH* and $a_{H_{2,\ aq}}$.

In contrast to the aqueous phase reaction in Fig. 12A, it can be seen in Fig. 12B that increasing pressure is predicted to favor a decrease in the ratio of CH_3COO^-/HCO_3^- in equilibrium with a fluid hydrocarbon that is pure methane. The reaction and the logarithm of the equilibrium constant here can be written as

$$CH_3COO^- + H_2O = HCO_3^- + CH_{4,f} \quad (11)$$

$$logK = log\left(\frac{a_{HCO_3^-}}{a_{CH_3COO^-}}\right) + log\left(a_{CH_{4,f}}\right) \quad (12)$$

As a fluid hydrocarbon appears very early in our experiments, this predicted behavior is overall consistent with our experimental observations, assuming that the activity of $a_{CH_{4,\ f}}$ in a mixture of hydrocarbons does not vary much compared with the variation of *logK* with pressure.

Values of $a_{H_{2,\ aq}}$ for the experiments can be derived from changes in

Table 2
Summary of the characteristics of the hydrocarbon fluids as a function of pressure at 300 °C. The uncertainties of the mole fraction of C-species are in the parathesis.

Expt. No.	P (GPa)	C mol% HC	Final pH at peak conditions	Average oxidation state of C in HC	Mole fraction of C-species in immiscible hydrocarbon fluids				Mole fraction of total C in immiscible hydrocarbon fluids			
					CH_4	C_2H_6	C_3H_8	C_4H_{10}	CH_4	C_2H_6	C_3H_8	C_4H_{10}
#7	1.6	33	6.70	−2.66	0.19(0.003)	nd	0.43(0.01)	0.38(0.01)	0.06	nd	0.43	0.51
#8	2.1	42	5.80	−2.95	0.57(0.04)	nd	0.18(0.004)	0.25(0.04)	0.27	nd	0.26	0.47
[a]	3.0	56	nd	−2.75	0.17	nd	nd	0.83	0.17	nd	nd	0.83
#0	3.4	39	4.29	−2.85	0.48(0.01)	0.05(0.001)	0.12(0.002)	0.35(0.01)	0.20	0.05	0.15	0.60
#6	4.6	53	4.58	−2.97	0.59(0.03)	nd	0.17(0.02)	0.24(0.01)	0.29	nd	0.24	0.47

[a] from Huang et al. (2017) for the Na-acetate system.

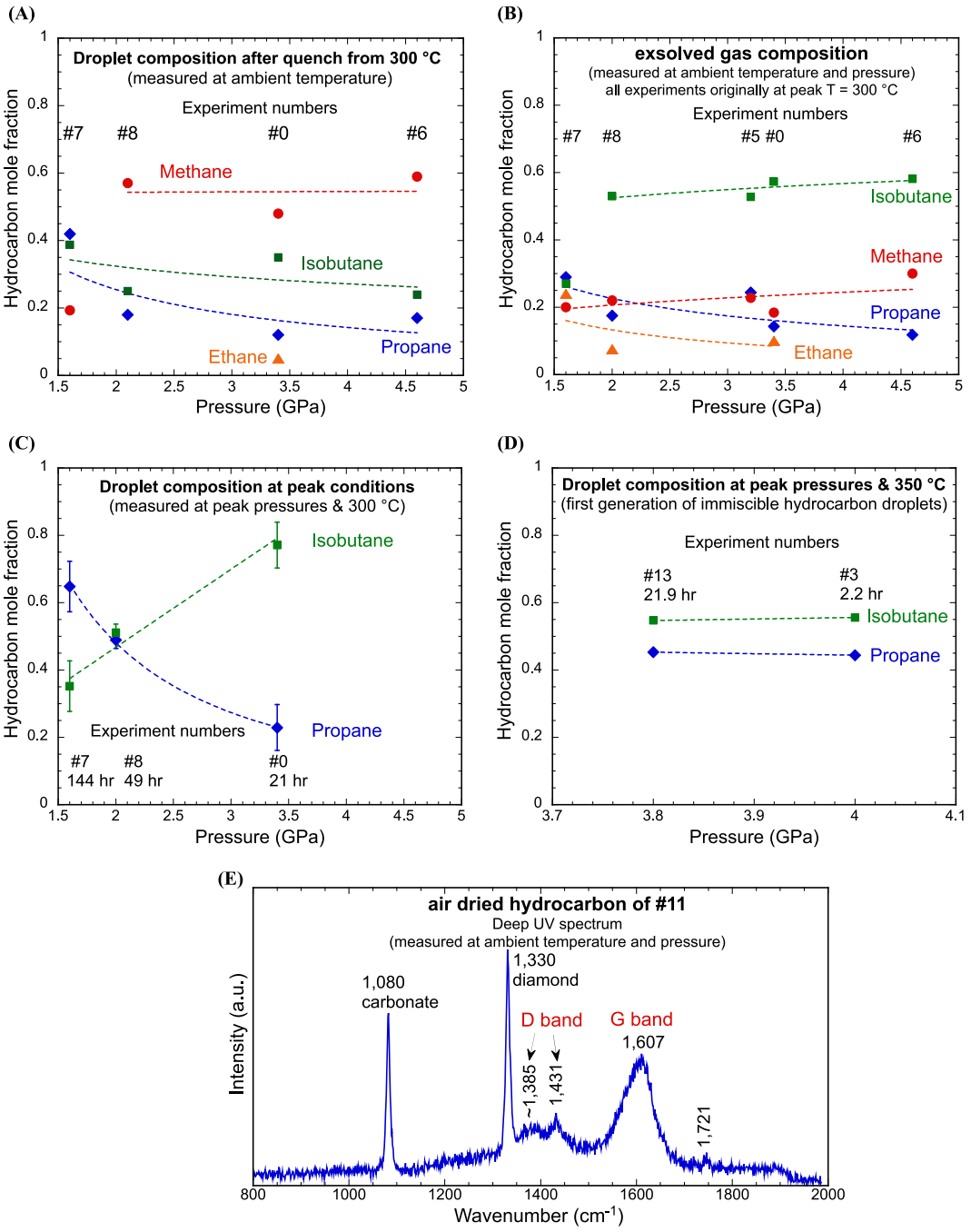

Fig. 9. Hydrocarbon composition as mole fractions based on ratios of Raman peak areas (see text). The dashed curves are guides for the eye: **(A)** quenched immiscible hydrocarbon; **(B)** the gas phase at 25 °C and near ambient pressure; **(C)** immiscible hydrocarbon at peak pressure and 300 °C; **(D)** first generation of immiscible hydrocarbon at peak pressure and 350 °C. **(E)** the deep UV Raman spectrum of the quenched second generation of refractory hydrocarbon in air, deposited on the diamond anvil.

the composition of the hydrocarbon fluid, as described next. For the hydrocarbon phase, as pressure increases from 1.6 to 4.6 GPa, there is an increase in the total amount of carbon in the hydrocarbon fluid. In addition, the composition of the hydrocarbon fluid changes with pressure, methane becoming the most abundant species at the highest pressure. Propane, which could be measured at peak conditions, is most abundant at the lowest pressure of 1.6 GPa. These changes in the composition of the hydrocarbon fluid with pressure suggest changes in the oxidation state of carbon in the hydrocarbon fluid. The carbon budgets detailed in Figs. 12A-C enable calculation of the average oxidation state of carbon in the hydrocarbon fluid with pressure, resulting in −2.66, −2.85, and − 2.97, as pressure increases from 1.6 to 3.4 to 4.6 GPa, respectively (Table 2). Clearly, the hydrocarbon fluid became more reduced with increasing pressure.

The observed trend with pressure for the composition of the hydrocarbon fluid can be studied theoretically by assuming equilibrium between the fluid hydrocarbon species, of which methane and propane are key indicators. The thermodynamic data summarized in Appendix A enable calculation of the equilibrium between fluid methane and fluid propane, assuming equilibrium with aqueous $H_{2,\,aq}$, according to

$$3CH_{4,f} = C_3H_{8,f} + 2H_{2,aq} \quad (13)$$

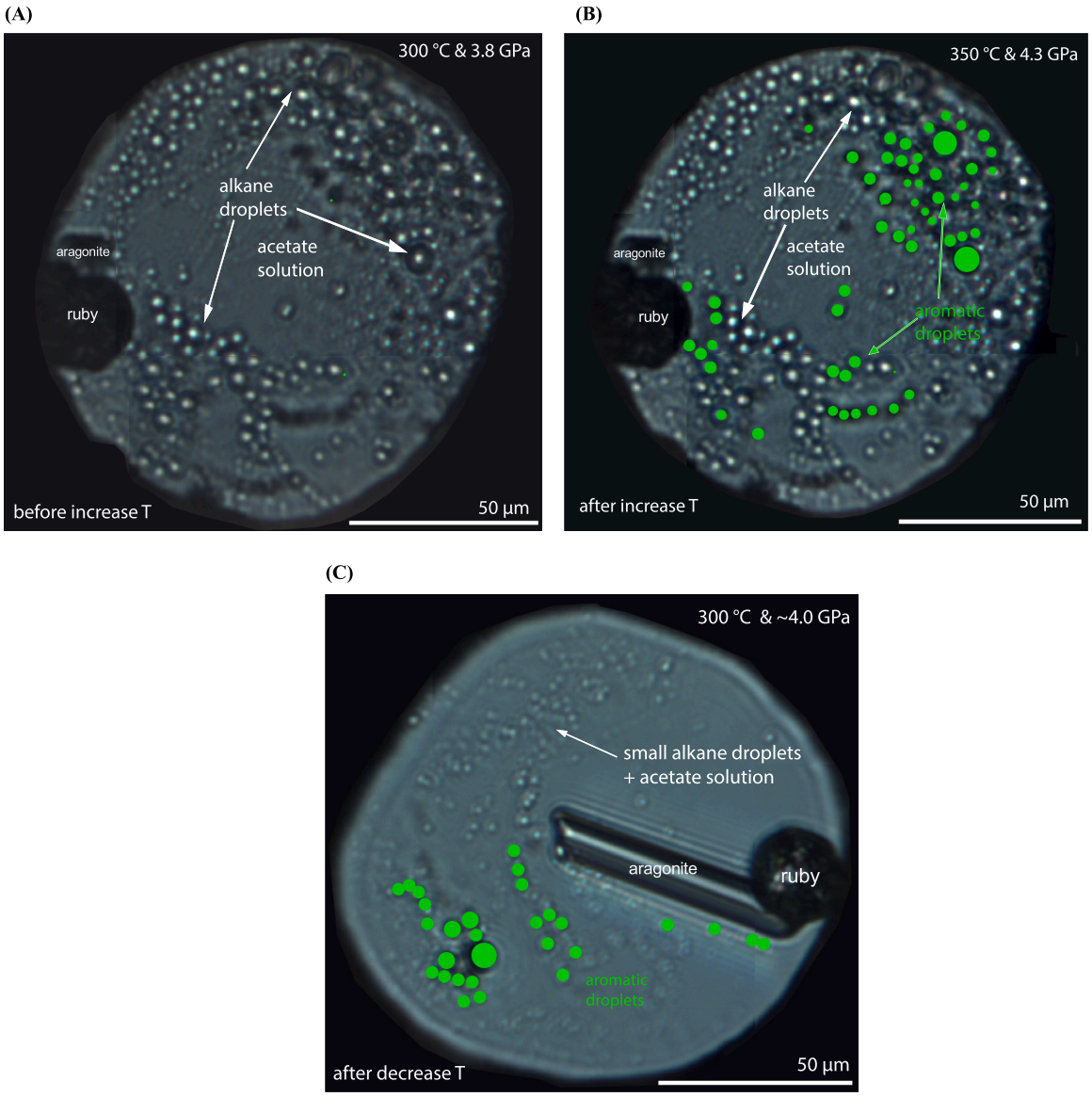

Fig. 10. The optical picture of Expt. #12 in transmitted light before **(A)** and after **(B)** increasing the temperature from 300 °C and 3.8 GPa to 4.3 GPa and 350 °C. **(C)** The optical picture of Expt. #13 at around 4.0 GPa after decreasing the temperature from 350 °C to 300 °C. The second generation of aromatic hydrocarbon droplets are colored in green. The first generation of immiscible alkane is remained with its natural brightness. (For interpretation of the references to colour in this figure legend, the reader is referred to the web version of this article.)

The logarithm of the equilibrium constant for this reaction can be written as

$$logK = log\left(\frac{a_{C_3H_{8,f}}}{\left(a_{CH_{4,f}}\right)^3}\right) + 2log\left(a_{H_{2,aq}}\right) \quad (14)$$

The predicted pressure and temperature dependence of *logK* is given in Fig. 12C where it can be seen that pure fluid methane is predicted to become more stable with increasing temperature and pressure. However, the specific stability of fluid methane relative to fluid propane as species in a hydrocarbon fluid is determined by the relative activities of the two hydrocarbon species and the value of the activity of aqueous $H_{2,aq}$, as can be seen by a re-arrangement of Eq. (14) above to give

$$\mathrm{Log}\left(a_{H_{2,aq}}\right) = 0.5logK - 0.5log\left(\frac{a_{C_3H_{8,f}}}{\left(a_{CH_{4,f}}\right)^3}\right) \quad (15)$$

For specified activity ratios of methane and propane, $\log(a_{H_{2,\,aq}})$ will be a function of pressure and temperature.

The predicted pressure and temperature dependence of $loga_{H_{2,\,aq}}$ is depicted in Fig. 12D, assuming a value of the ratio of $\frac{a_{C_3H_{8,f}}}{\left(a_{CH_{4,f}}\right)^3}$ equal to unity. At 300 °C, rather low values of $\log(a_{H_{2,\,aq}})$ are predicted for the experimental pressures of this study. For example, at 1.6, 2.1, 3.4, and 4.6 GPa, values of $\log(a_{H_{2,\,aq}})$ are predicted to be −6.1, −6.6, −8.3, and − 10.1, respectively. Interestingly, using the hydrocarbon mole fractions given in Table 2 and Fig. 9C gives very similar results; the corresponding values of $loga_{H_{2,\,aq}}$ are −7.0, −6.6, −8.3, and − 10.0 at 1.6, 2.1, 3.4, and 4.6 GPa. This result suggests that the components of the hydrocarbon fluid may be close to equilibrium (or metastable equilibrium) during the experiments.

4.4. The formation of immiscible aromatic hydrocarbon fluids at 350 °C

In experiments performed at 350 °C, aromatic hydrocarbons formed, causing strong fluorescence that hindered Raman measurements and remained after quenching. In expt. #10 at 2.4 GPa, a small peak of

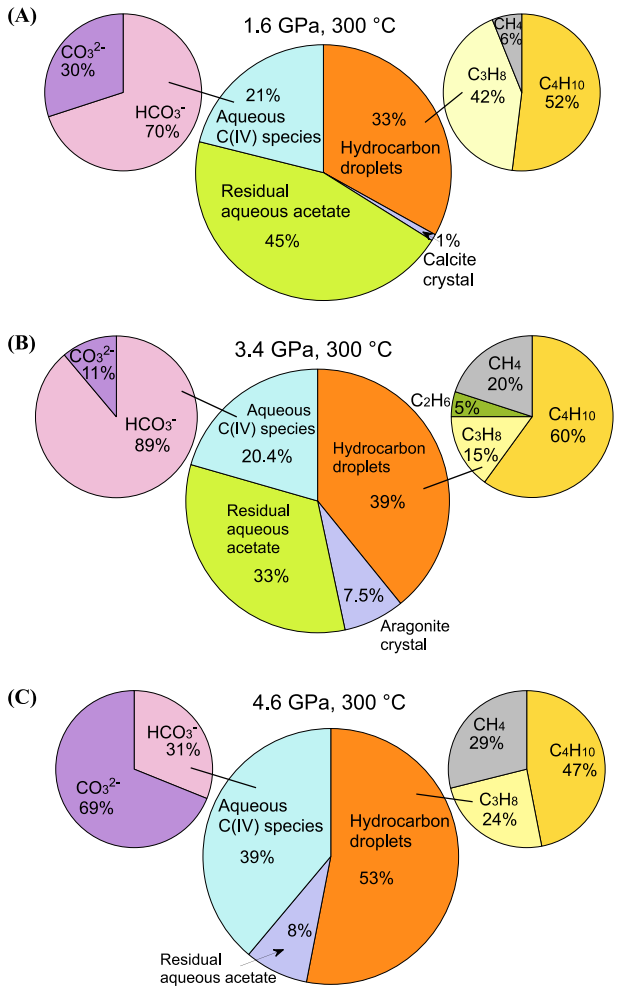

Fig. 11. Carbon budget at **(A)** 300 °C and 1.6 GPa (Expt. #7) **(B)** 300 °C and 3.4 GPa (Expt. #0), **(C)** 300 °C and 4.6 GPa (Expt. #6). The center pie graph represents the overall budget of carbon at peak conditions, the left pie graph represents the composition of aqueous C(IV) species at peak conditions, and the right pie graph represents the composition of immiscible liquid hydrocarbon droplets measured after quench. The percentages represent mol% of the total carbon in the cell.

isobutane was detected. In experiments varying the temperature at around 3.5 and 4.3 GPa, the largest droplets of alkanes turned to aromatic droplets after the temperature was increased from 300 to 350 °C, which persisted after decreasing the temperature from 350 to 300 °C. The aromatic droplets could not be measured by *in situ* UV Raman spectroscopy due to the strong absorption by the diamond anvil in the UV range. They were measured after the cell was opened and show similarities to bitumen.

The formation of aromatic hydrocarbons from alkanes under hydrothermal conditions has previously been documented by a group of experiments involving dehydrogenation, dehydration, metal oxidation and disproportionation reactions (Shipp et al., 2013; Yang et al., 2015, 2018; Venturi et al., 2017; Fecteau et al., 2019; Shock et al., 2019). Unlike aromatization experiments at ambient condition, which use palladium as a catalyst in a strong Lewis acid environment, the experiments under hydrothermal conditions simply used water and common minerals such as sphalerite (*ZnS*). Water becomes a strong solvent of organics at high temperature because of the dramatic decrease of the dielectric constant (Shock et al., 2019). For example, in experiments at 300 °C and pressure at the liquid-vapor saturation curve of water (Psat) starting with aqueous cyclohexane with or without minerals of sphalerite, hematite, magnetite and quartz, benzene formed after 10 days. Cyclohexene and cyclohexadiene also formed, possibly as intermediate products. In presence of sphalerite, a small amount of phenol also formed (Venturi et al., 2017). The minerals were suggested to act as reversible catalysts for dehydrogenation of cyclopentane.

Thermodynamic calculations provided an explanation of the dehydrogenation of aqueous cyclopentane at Psat hydrothermal condition to form aqueous benzene and aqueous hydrogen (Shock and Helgeson, 1990; Shock et al., 1992, 2019). The chemical reaction can be written as

$$C_6H_{12,aq} = C_6H_{6,aq} + 3H_{2,aq} \tag{16}$$

and the logarithm of the equilibrium constant (*logK*) can be written as

$$logK = log\left(\frac{a_{C_6H_{6,aq}}}{a_{C_6H_{12,aq}}}\right) + 3log\left(a_{H_{2,aq}}\right) \tag{17}$$

The log*K* of this reaction increases with temperature in Eq. (17), which favors the formation of benzene at low activities of hydrogen. With increasing temperature, the entropic change becomes dominant over the enthalpic change, and causes an increase of log*K*.

Although our experimental conditions are at much higher pressures, there are multiple reasons to suggest dehydrogenation could form aromatic compounds from small alkane molecules of C4. First, water could be an even stronger solvent at pressures of a few GPa. Second, immiscible alkane droplets provide highly concentrated spots of reactants consistent with the observation that aromatics replaced the big droplets first. Third, the dehydrogenation is favored by high temperature thermodynamically, and this is consistent with the observations that aromatics only form at 350 °C and above. Although the identity of the aromatic hydrocarbon in our experiments is yet unknown, we can illustrate the formation of aromatics using two reactions forming the simplest fluid aromatic hydrocarbons, benzene and toluene, from fluid propane and isobutane, according to

$$2C_3H_{8,f} = C_6H_{6,f} + 5H_{2,aq} \tag{18}$$

$$C_3H_{8,f} + isoC_4H_{10,f} = C_7H_{8,f} + 5H_{2,aq} \tag{19}$$

the logarithms of the equilibrium constant (*logK*) for each reaction can be written as

$$logK = log\left(\frac{a_{C_6H_{6,f}}}{a_{C_6H_{12,f}}}\right) + 5log\left(a_{H_{2,aq}}\right) \tag{20}$$

and

$$logK = log\left(\frac{a_{C_7H_{8,f}}}{\left(a_{C_3H_{8,f}}\right)\left(a_{isoC_4H_{10,f}}\right)}\right) + 5log\left(a_{H_{2,aq}}\right) \tag{21}$$

The predicted $loga_{H_{2,\ aq}}$ of the two reactions are calculated as 1/5 of log*K*, assuming a value of the ratios of $\frac{a_{C_6H_{6,f}}}{\left(a_{C_3H_{8,f}}\right)^2}$ and $\frac{a_{C_7H_{8,f}}}{\left(a_{C_3H_{8,f}}\right)\left(a_{isoC_4H_{10,f}}\right)}$ equal to unity, *i.e.* pure fluid hydrocarbons. The $loga_{H_{2,\ aq}}$ values are presented from 300 to 550 °C and 0.5 to 5.0 GPa in Fig. 13. High temperature, low pressure and low $loga_{H_{2,\ aq}}$ conditions favor the formation of fluid benzene and toluene. Also, note that the effect of temperature increases with pressure. The $loga_{H_{2,\ aq}}$ values required to form toluene are slightly higher than for benzene. These calculations give some support to the experimental finding that higher temperature could be a reason for the transformation of alkanes to aromatics.

4.5. Geological implications

Our experiments at 300 and 350 °C and over a wide range of pressures indicate that the decomposition of acetate has several potential implications for reactions at subduction zone conditions. First, increasing pressure from 1.6 to 4.6 GPa favors greater amounts of decarboxylation to produce an immiscible hydrocarbon-bearing fluid.

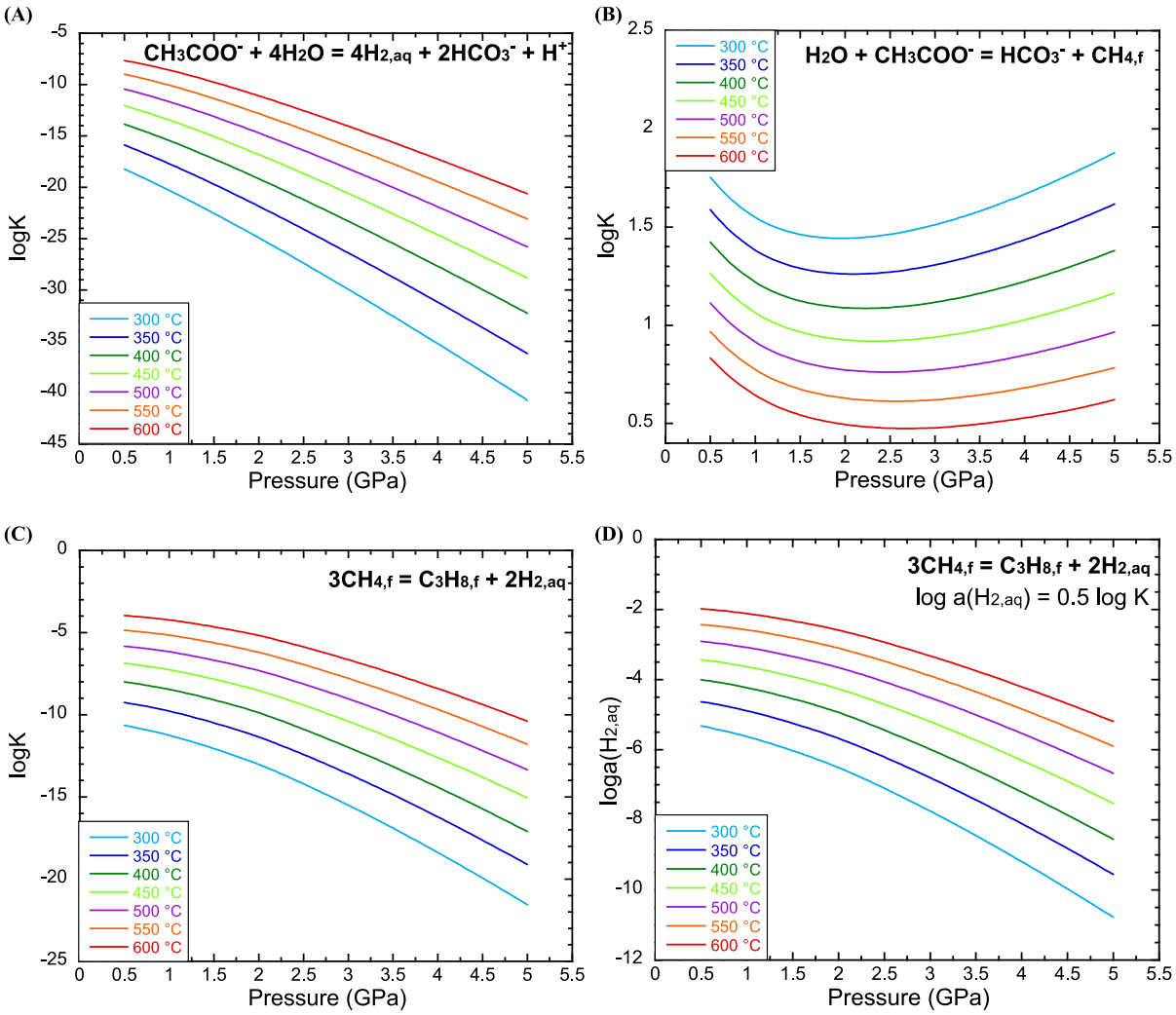

Fig. 12. Theoretical prediction of equilibria involving aqueous and aliphatic fluid hydrocarbons as a function of pressure using the DEW model for aqueous species and gases, and fugacity coefficients for methane and propane from 0.5 to 5.0 GPa and from 300 to 600 °C: **(A)** The logarithm of the equilibrium constant of aqueous acetate and bicarbonate; **(B)** The logarithm of the equilibrium constant of aqueous acetate decarboxylation to fluid methane; **(C)** The logarithm of the equilibrium constant for fluid methane, propane, and $H_{2,\ aq}$; **(D)** The logarithm of the activity of $H_{2,\ aq}$ in equilibrium with fluid methane and propane with activities equal to unity.

Second, the immiscible hydrocarbon-bearing fluid consisted of variable proportions of alkanes including methane, ethane, propane, butane, and isobutane between 1.6 and 4.6 GPa; Experiments at 350 °C showed the transformation some of the alkanes to an immiscible fluid likely consisting of one or more aromatic hydrocarbons. Thirdly, thermodynamic calculations show that decarboxylation of acetate to form aqueous methane are opposed with pressure; however, reactions forming fluid methane are favored at high pressure at 2.0–5.0 GPa (Fig. 12B). Also, aqueous butane formation from methane is favored with pressure (Huang et al., 2017). Moreover, in an experiment performed at 3 GPa and 550 °C with buffered f_{O2} of QFM + 0.61 of synthetic ^{13}C-aragonite and ^{12}C-graphite reacting with water, the isotopic composition of CO_2 reflected the oxidation of graphite which means that graphite reactivity with aqueous fluids controlled the reaction (Tumiati et al., 2022). Overall, our results suggest that at subduction zone conditions, if graphite formation is kinetically inhibited, immiscible fluid hydrocarbons may form metastably instead of graphite over a wide range of pressures at moderate temperatures of 300–350 °C.

Geological observations show that immiscible methane-rich hydrocarbon fluids have formed under subduction zone conditions. For example, fluid inclusions of $CH_4 - H_2$ were found in the carbon-bearing metamorphosed ophicarbonates from the Lanzo Alpine Massifs, western Italy (Vitale Brovarone et al., 2017). The conditions at which these formed were about 400 °C at 15–40 km depth. Graphite and $CH_4 - C_2H_6$ fluid inclusions were found in carbonated eclogite from Tianshan, the northwest of China (Tao et al., 2018). The depth at which those inclusions formed was about 80 km (~2.5 GPa), at about 500 °C, and the logf_{O2} was about QFM −2.5 log units. In addition, at similar P-T conditions in south or southwest of Tianshan, China, CH_4-rich fluid inclusions were found in zoned garnet from eclogites (Zhang et al., 2023), and in ultra-high-pressure eclogites from a palaeosubduction zone (Wang et al., 2022). Together with the results of our experiments, these field and laboratory studies strongly suggest that processes involving abiotic immiscible fluid hydrocarbons might be important in subduction zones over a wide range of pressures and depths.

5. Conclusions

Experiments performed from 1.6 to 4.6 GPa, and 300 and 350 °C, starting with 0.5 M Ca-acetate solutions, showed the decomposition of acetate into aqueous HCO_3^- and CO_3^{2-} in the aqueous solution, calcite or aragonite crystals, and immiscible hydrocarbon fluids. The major conclusions from our experiments and calculations are as follows:

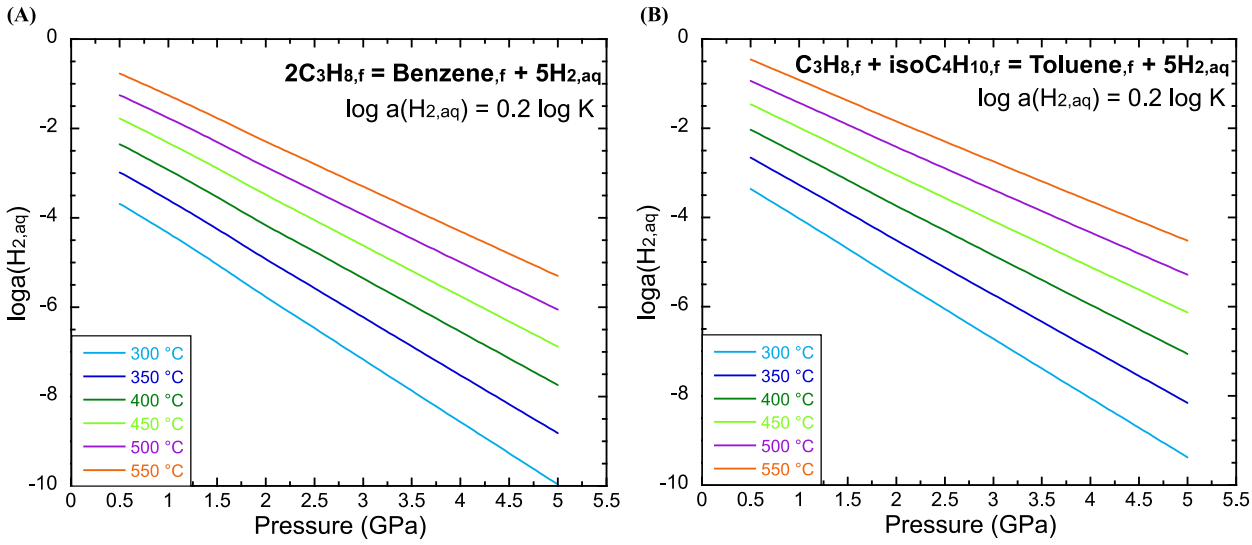

Fig. 13. Theoretical prediction of equilibria involving aqueous hydrogen and aromatic fluid hydrocarbons as a function of pressure using the DEW model for aqueous species and gas, and fugacity coefficients for fluid hydrocarbons from 0.5 to 5.0 GPa and from 300 to 550 °C: the logarithm of the activity of $H_{2,\ aq}$ in equilibrium with hydrocarbon activities equal to unity of fluid propane to benzene **(A)**, and of fluid propane and isobutane to toluene **(B)**.

(1) In the aqueous solution, the peak area ratio of $CH_3COO^-/(1+n)$ HCO_3^- decreased systematically with time and was strongly affected by pressure and temperature. High pressure and high temperature accelerated the decomposition of acetate with more acetate reacting with increasing pressure. The final pH of the solution decreased as a function of pressure, but increased slightly at the highest pressure at 4.6 GPa where aragonite did not precipitate.

(2) High-pressure favored the formation of alkane hydrocarbon fluids consisting mainly of methane, propane and isobutane at 300 °C. The mole fractions of isobutane and propane decreased with pressure, whilst methane increased. Because of different numbers of moles of carbon in the different hydrocarbon molecules, in the mole percentage of the total C in the system, isobutane stays around 50%, while propane decreases, and methane increases. Compared with previous Na-acetate experiments (Huang et al., 2017), our immiscible hydrocarbon fluids formed at similar pressure contain much less isobutane but more methane and propane as mole fractions of the hydrocarbon fluid. Interestingly, the overall oxidation states of the hydrocarbon fluids are similar. Compared with the previous Na-formate experiments with buffered f_{O2} at higher temperature (Li, 2017), no graphite ever formed in our experiments, probably due to kinetic inhibition at our experimental temperatures. Progress in our experiments shows that the formation of hydrocarbons is promoted by higher pressures at a given temperature.

(3) At 350 °C, immiscible fluorescent droplets formed after the initial formation of isobutane droplets. In Expt. #12, the largest alkane droplets immediately became fluorescent after the temperature increased from 300 to 350 °C; small alkane droplets stayed non-fluorescent and co-existed with the aqueous solution until the end of the experiment. The transition from alkane to aromatic hydrocarbons was not reversible with decreasing temperature.

(4) Thermodynamic calculations showed that forming pure fluid methane is favored with pressure but opposed by temperature, which is opposite to the trend forming aqueous H_2. Consistent with experimental results, fluid methane is favored over propane and aqueous H_2 with pressure. The activity of aqueous H_2 decreased with pressure.

Overall, our study strongly suggests that hydrocarbons could form over a wide range of pressures at subduction zone conditions and could perhaps play an important role in the deep carbon cycle. Further experimental and modelling studies could explore the conditions under which different immiscible hydrocarbon fluids might be either metastable or stable relative to graphite and diamond under subduction-zone conditions.

Declaration of Competing Interest

The authors declare that they have no known competing financial interests or personal relationships that could have appeared to influence the work reported in this paper.

Data availability

Data will be made available on request.

Acknowledgements

This research was supported by a Johns Hopkins Graduate Fellowship, the NSF Grant #2032039, and DOE Grant #DE-SC0019830. We thank Fang Huang for providing much help in the calculation of the carbon budget and Renbiao Tao for help in the analysis of the Raman spectra. We also thank Emmanuelle Albalat at the ENS de Lyon for measuring the Ca concentration in the residual aragonite crystals after the experiments by ICP-MS. We thank Everett Shock for discussion about thermodynamic properties of aromatic hydrocarbons. The Raman facility at the ENS de Lyon is supported by the Institut National des Sciences de l'Univers (INSU) and by the LABEX Lyon Institute of Origins (ANR-10-LABX-0066). We are grateful to Simone Tumiati and one anonymous reviewer for their insightful and constructive comments and to Claudia Romano (Editor-in-Chief) for her careful editorial handling and helpful suggestions.

Appendix A. Supplementary data

Supplementary data to this article can be found online at https://doi.org/10.1016/j.chemgeo.2023.121489.

References

Boutier, A., Vitale, Brovarone A., Martinez, I., Sissmann, O., Mana, S., 2021. High-pressure serpentinization and abiotic methane formation in metaperidotite from the Appalachian subduction, northern Vermont. Lithos 396–397, 106190.

Chervin, J.C., Canny, B., Besson, J.M., Pruzan, P., 1995. A diamond anvil cell for IR microspectroscopy. Rev. Sci. Instrum. 66, 2595–2598.

Chervin, J.C., Canny, B., Mancinelli, M., 2001. Ruby-spheres as pressure gauge for optically transparent high pressure cells. High Pressure Res. 21, 305–314.

Etiope, G., Sherwood, Lollar B., 2013. Abiotic methane on earth. Rev. Geophys. 51, 276–299.

Facq, S., Daniel, I., Montagnac, G., Cardon, H., Sverjensky, D.A., 2014. In situ Raman study and thermodynamic model of aqueous carbonate speciation in equilibrium with aragonite under subduction zone conditions. Geochim. Cosmochim. Acta 132, 375–390.

Facq, S., Daniel, I., Montagnac, G., Cardon, H., Sverjensky, D.A., 2016. Carbon speciation in saline solutions in equilibrium with aragonite at high pressure. Chem. Geol. 431, 44–53.

Fecteau, K.M., Gould, I.R., Glein, C.R., Williams, L.B., Hartnett, H.E., Shock, E.L., 2019. Production of carboxylic acids from aldehydes under hydrothermal conditions: A kinetics study of benzaldehyde. ACS Earth Space Chem. 3, 170–191.

Foustoukos, D.I., 2012. Metastable equilibrium in the C-H-O system: Graphite deposition in crustal fluids. Am. Mineral. 97, 1373–1380.

Foustoukos, D.I., Stern, J.C., 2012. Oxidation pathways for formic acid under low temperature hydrothermal conditions: Implications for the chemical and isotopic evolution of organics on Mars. Geochim. Cosmochim. Acta 76, 14–28.

Frantz, J.D., 1998. Raman spectra of potassium carbonate and bicarbonate aqueous fluids at elevated temperatures and pressures: Comparison with theoretical simulations. Chem. Geol. 152, 211–225.

Frezzotti, M.L., 2019. Diamond growth from organic compounds in hydrous fluids deep within the Earth. Nat. Commun. 10.

Glein, C.R., Gould, I.R., Lorance, E.D., Hartnett, H.E., Shock, E.L., 2020. Mechanisms of decarboxylation of phenylacetic acids and their sodium salts in water at high temperature and pressure. Geochim. Cosmochim. Acta 269, 597–621.

Gold, T., 1992. The deep, hot biosphere. Proc. Natl. Acad. Sci. U. S. A. 89, 6045–6049.

Gold, T., 2001. The Deep Hot Biosphere: The Myth of Fossil Fuels. Springer Science & Business Media.

Helgeson, H.C., Knox, A.M., Owens, C.E., Shock, E.L., 1993. Petroleum, oil field waters, and authigenic mineral assemblages are they in metastable equilibrium in hydrocarbon reservoirs. Geochim. Cosmochim. Acta 57, 3295–3339.

Helgeson, H.C., Owens, C.E., Knox, A.M., Richard, L., 1998. Calculation of the standard molal thermodynamic properties of crystalline, liquid, and gas organic molecules at high temperatures and pressures. Geochim. Cosmochim. Acta 62, 985–1081.

Helgeson, H.C., Richard, L., McKenzie, W.F., Norton, D.L., Schmitt, A., 2009. A chemical and thermodynamic model of oil generation in hydrocarbon source rocks. Geochim. Cosmochim. Acta 73, 594–695.

Hollis, J.R., Abbey, W., Beegle, L.W., Bhartia, R., Ehlmann, B.L., Miura, J., Monacelli, B., Moore, K., Nordman, A., Scheller, E., Uckert, K., Wu, Y., 2021. A deep-ultraviolet Raman and Fluorescence spectral library of 62 minerals for the SHERLOC instrument onboard Mars 2020. Planet Space Sci. 209, 105356.

Huang, F., Daniel, I., Cardon, H., Montagnac, G., Sverjensky Di, A., 2017. Immiscible hydrocarbon fluids in the deep carbon cycle. Nat. Commun. 8.

Hunt, J.M., 1995. Petroleum Geochemistry and Geology (Textbook), 2nd ed. WH Freeman Company.

Journaux, B., Daniel, I., Caracas, R., Montagnac, G., Cardon, H., 2013. Influence of NaCl on ice VI and ice VII melting curves up to 6 GPa, implications for large icy moons. Icarus 226, 355–363.

Kenney, J.F., Kutcherov, V.A., Bendeliani, N.A., Alekseev, V.A., 2002. The evolution of multicomponent systems at high pressures: VI. The thermodynamic stability of the hydro-carbon system: the genesis of hydrocarbons and the origin of petroleum. Proc. Natl. Acad. Sci. 99, 10976–10981.

Kolesnikov, A.Y., Saul, J.M., Kutcherov, V.G., 2017. Chemistry of Hydrocarbons under Extreme Thermobaric Conditions. ChemistrySelect 2, 1336–1352.

Kropotkin, P.N., 1997. On the history of science professor NA koudryavtsev (1893–1971) and the development of the theory of origin of oil and gas. Earth Sci. History 16, 17–20.

Kudryavtsev, N.A., 1959. Geological proof of the deep origin of petroleum. In: *Trudy Vsesoyuz.* Neftyan. Nauch. Issledovatel Geologoraz Vedoch. Inst, 132, pp. 242–262.

Li, Y., 2017. Immiscible CHO fluids formed at subduction zone conditions. Geochem. Pespect. Lett 3, 12–21.

Lijuan, Zhang, Lifei, Zhang, Tang, M., Wang, X., Tao, R., Xu, C., Bader, T., 2023. Massive abiotic methane production in eclogite during cold subduction. Natl. Sci. Rev. 10.

Lobanov, S.S., Chen, P.N., Chen, X.J., Zha, C.S., Litasov, K.D., Mao, H.K., Goncharov, A. F., 2013. Carbon precipitation from heavy hydrocarbon fluid in deep planetary interiors. Nat. Commun. 4, 1–8.

Luque, F.J., Ortega, L., Barrenechea, J.F., Millward, D., Beyssac, O., Huizenga, J.M., 2009. Deposition of highly crystalline graphite from moderate-temperature fluids. Geology 37, 275–278.

Manning, C.E., Shock, E.L., Sverjensky, D.A., 2013. The chemistry of carbon in aqueous fluids at crustal and upper-mantle conditions: Experimental and theoretical constraints. Rev. Mineral. Geochem. 75, 109–148.

McCollom, T.M., 2013. Laboratory simulations of abiotic hydrocarbon formation in earth's deep subsurface. Rev. Mineral. Geochem. 75, 467–494.

McCollom, T.M., Seewald, J.S., 2003a. Experimental constraints on the hydrothermal reactivity of organic acids and acid anions: I. Formic acid and formate. Geochim. Cosmochim. Acta 67, 3625–3644.

McCollom, T.M., Seewald, J.S., 2003b. Experimental study of the hydrothermal reactivity of organic acids and acid anions: II. Acetic acid, acetate, and valeric acid. Geochim. Cosmochim. Acta 67, 3645–3664.

Mendeleev, D., 1877. L'origine du petrole. Revue Sci. 2e Ser, 409–416.

Milesi, V., Guyot, F., Brunet, F., Richard, L., Recham, N., Benedetti, M., Dairou, J., Prinzhofer, A., 2015. Formation of CO2, H2 and condensed carbon from siderite dissolution in the 200–300 C range and at 50 MPa. Geochim. Cosmochim. Acta 154, 201–211.

Pan, D., Galli, G., 2020. A first principles method to determine speciation of carbonates in supercritical water. Nat. Commun. 11, 1–6.

Peng, W., Zhang, L., Tumiati, S., Vitale, Brovarone A., Hu, H., Cai, Y., Shen, T., 2021. Abiotic methane generation through reduction of serpentinite-hosted dolomite: Implications for carbon mobility in subduction zones. Geochim. Cosmochim. Acta 311, 119–140.

Peng, W., Tumiati, S., Zhang, L., Tiraboschi, C., Vitale, Brovarone A., Toffolo, L., Poli, S., 2022. An experimental study on kinetics-controlled ca-carbonate aqueous reduction into CH4 (1 and 2 GPa, 550°C): implications for C mobility in subduction zones. J. Petrol. 63, egac070.

Quirico, E., Bonal, L., Montagnac, G., Beck, P., Reynard, B., 2020. ScienceDirect New insights into the structure and formation of coals, terrestrial and extraterrestrial kerogens from resonant UV Raman spectroscopy. Geochim. Cosmochim. Acta 282, 156–176.

Schmidt, C., 2014. Raman spectroscopic determination of carbon speciation and quartz solubility in H2O+Na2CO3 and H2O+NaHCO3 fluids to 600°C and 1.53GPa. Geochim. Cosmochim. Acta 145, 281–296.

Scott, H.P., Hemley, R.J., Mao, H.K., Herschbach, D.R., Fried, L.E., Howard, W.M., Bastea, S., 2004. Generation of methane in the Earth's mantle: in situ high pressure-temperature measurements of carbonate reduction. Proc. Natl. Acad. Sci. U. S. A. 101, 14023–14026.

Seewald, J.S., 1994. Evidence for metastable equilibrium between hydrocarbons under hydrothermal conditions. Nature 370, 285–287.

Seewald, J.S., Zolotov, M.Y., McCollom, T., 2006. Experimental investigation of single carbon compounds under hydrothermal conditions. Geochim. Cosmochim. Acta 70, 446–460.

Shipp, J., Gould, I.R., Herckes, P., Shock, E.L., Williams, L.B., Hartnett, H.E., 2013. Organic functional group transformations in water at elevated temperature and pressure: Reversibility, reactivity, and mechanisms. Geochim. Cosmochim. Acta 104, 194–209.

Shock, E.L., 1990. Geochemical constraints on the origin of organic compounds in hydrothermal systems. Orig. Life Evol. Biosph. 20, 331–367.

Shock, E.L., 1992. Chemical environments of submarine hydrothermal systems. Marine Hydrothermal Syst. Origin Life 67–107.

Shock, E.L., 1994. Application of thermodynamic calculations to geochemical processes involving organic acids. In: Organic Acids in Geological Processes. Springer, pp. 270–318.

Shock, E.L., Helgeson, H.C., 1990. Calculation of the thermodynamic and transport properties of aqueous species at high pressures and temperatures: Standard partial molal properties of organic species. Geochim. Cosmochim. Acta 54, 915–945.

Shock, E.L., Schulte, M.D., 1998. Organic synthesis during fluid mixing in hydrothermal systems. J. Geophys. Res. E: Planets 103, 28513–28527.

Shock, E.L., Oelkers, E.H., Johnson, J.W., Sverjensky, D.A., Helgeson, H.C., 1992. Calculation of the thermodynamic properties of aqueous species at high pressures and temperatures. Effective electrostatic radii, dissociation constants and standard partial molal properties to 1000 C and 5 kbar. J. Chem. Soc. Faraday Trans. 88, 803–826.

Shock, E., Bockisch, C., Estrada, C., Fecteau, K., Gould, I.R., Hartnett, H., Johnson, K., Robinson, K., Shipp, J., Williams, L., 2019. Earth as Organic Chemist.

Sobolev, N.V., Tomilenko, A.A., Bul'bak, T.A., Logvinova, A.M., 2019. Composition of hydrocarbons in diamonds, garnet, and olivine from diamondiferous peridotites from the Udachnaya Pipe in Yakutia, Russia. Engineering 5, 471–478.

Syracuse, E.M., van Keken, P.E., Abers, G.A., Suetsugu, D., Bina, C., Inoue, T., Wiens, D., Jellinek, M., 2010. The global range of subduction zone thermal models. Phys. Earth Planet. Inter. 183, 73–90.

Szlachta, V., Vlasov, K., Keppler, H., 2022. On the Stability of Acetate in Subduction Zone Fluids, pp. 28–31.

Tao, R., Zhang, L., Tian, M., Zhu, J., Liu, X., Liu, J., Höfer, H.E., Stagno, V., Fei, Y., 2018. Formation of abiotic hydrocarbon from reduction of carbonate in subduction zones: Constraints from petrological observation and experimental simulation. Geochim. Cosmochim. Acta 239, 390–408.

Toffolo, L., Tumiati, S., Villa, A., Fumagalli, P., Amalfa, A., Miozzi, F., 2023. Experimental dissolution of carbonaceous materials in water at 1 GPa and 550°C: Assessing the role of carbon forms and redox state on COH fluid production and composition during forearc subduction of organic matter. Front. Earth Sci. (Lausanne) 11.

Tumiati, S., Recchia, S., Remusat, L., Tiraboschi, C., Sverjensky, D.A., Manning, C.E., Vitale, Brovarone A., Boutier, A., Spanu, D., Poli, S., 2022. Subducted organic matter buffered by marine carbonate rules the carbon isotopic signature of arc emissions. Nat. Commun. 13.

Venturi, S., Tassi, F., Gould, I.R., Shock, E.L., Hartnett, H.E., Lorance, E.D., Bockisch, C., Fecteau, K.M., Capecchiacci, F., Vaselli, O., 2017. Mineral-assisted production of benzene under hydrothermal conditions: Insights from experimental studies on C6 cyclic hydrocarbons. J. Volcanol. Geotherm. Res. 346, 21–27.

Vitale Brovarone, A., Martinez, I., Elmaleh, A., Compagnoni, R., Chaduteau, C., Ferraris, C., Esteve, I., 2017. Massive production of abiotic methane during subduction evidenced in metamorphosed ophicarbonates from the Italian Alps. Nat. Commun. 8, 1–13.

Vitale Brovarone, A., Sverjensky, D.A., Piccoli, F., Ressico, F., Giovannelli, D., Daniel, I., 2020. Subduction hides high-pressure sources of energy that may feed the deep subsurface biosphere. Nat. Commun. 11, 1–11.
Wang, C., Tao, R., Walters, J.B., Höfer, H.E., Zhang, L., 2022. Favorable P–T–fO_2 conditions for abiotic CH_4 production in subducted oceanic crusts: A comparison between CH_4-bearing ultrahigh- and CO_2-bearing high-pressure eclogite. Geochim. Cosmochim. Acta 336, 269–290.
Yang, J., Meng, F., Xu, X., Robinson, P.T., Dilek, Y., Makeyev, A.B., Wirth, R., Wiedenbeck, M., Cliff, J., 2015. Diamonds, native elements and metal alloys from chromitites of the Ray-Iz ophiolite of the Polar Urals. Gondwana Res. 27, 459–485.
Yang, Z., Gould, I.R., Williams, L.B., Hartnett, H.E., Shock, E.L., 2018. Effects of iron-containing minerals on hydrothermal reactions of ketones. Geochim. Cosmochim. Acta 223, 107–126.